



The COS CGM Compendium. I. Survey Design and Initial Results

Nicolas Lehner¹, Christopher B. Wotta¹, J. Christopher Howk¹, John M. O’Meara²,
Benjamin D. Oppenheimer³, and Kathy L. Cooksey⁴

¹ Department of Physics, University of Notre Dame, Notre Dame, IN 46556, USA

² Department of Chemistry and Physics, Saint Michael’s College, Colchester, VT 05439, USA

³ CASA, Department of Astrophysical and Planetary Sciences, University of Colorado, Boulder, CO 80309, USA

⁴ Department of Physics and Astronomy, University of Hawai’i at Hilo, HI 96720, USA

Received 2018 April 24; revised 2018 July 27; accepted 2018 August 15; published 2018 October 8

Abstract

We present a neutral hydrogen-selected absorption-line survey of gas with H I column densities $15 < \log N_{\text{HI}} < 19$ at $z \lesssim 1$ using the Cosmic Origins Spectrograph on the *Hubble Space Telescope*. Our main aim is to determine the metallicity distribution of these absorbers. Our sample consists of 224 absorbers selected on the basis of their H I absorption strength. Here we discuss the properties of our survey and the immediate empirical results. We find singly and doubly ionized metal species, and H I typically have similar velocity profiles, implying they probe gas in the same or similar environments. The ionic ratios (e.g., $N_{\text{C II}}/N_{\text{C III}}$, $N_{\text{O I}}/N_{\text{C II}}$) indicate that the gas in these absorbers is largely ionized, and the ionization conditions are quite comparable across the sampled N_{HI} range. The Doppler parameters of the H I imply $T \lesssim 5 \times 10^4$ K on average, consistent with the gas being photoionized. The Mg II column densities span >2 orders of magnitude at any given N_{HI} , indicating a wide range of metallicities (from solar to $<1/100$ solar). In the range of $16.2 \lesssim \log N_{\text{HI}} \lesssim 17$, there is a gap in the $N_{\text{Mg II}}$ distribution corresponding to gas with $\sim 10\%$ solar metallicity, consistent with the gap seen in the previously identified bimodal metallicity distribution in this column density regime. Less than 3% of the absorbers in our sample show no detectable metal absorption, implying that truly pristine gas at $z \lesssim 1$ is uncommon. We find $\langle [\text{Fe II}/\text{Mg II}] \rangle = -0.4 \pm 0.3$, and since α -enhancement can affect this ratio, dust depletion is extremely mild.

Key words: galaxies: abundances – galaxies: halos – quasars: absorption lines

Supporting material: figure set, machine-readable tables

1. Introduction

Modern theory and cosmological simulations agree that the star formation of galaxies and the properties of their circumgalactic medium (CGM) should be intimately connected (see recent review by Tumlinson et al. 2017). This is especially true for the flows through the CGM: feedback from star formation is understood to drive outflows that carry mass and metals away from galaxies, while infall from the intergalactic medium (IGM) is thought to bring in fresh gas to fuel ongoing star formation. Without significant feedback, most baryons would cool into the centers of halos to form prodigious quantities of stars (e.g., White & Rees 1978; Kereš et al. 2009), but with feedback, the baryon content of stars and cold gas in galaxies can be matched by driving matter into the CGM and beyond (e.g., Fukugita et al. 1998; Conroy & Wechsler 2009). Similarly, without continued infall of IGM material, star-forming galaxies would consume their interstellar gas in ~ 1 Gyr (e.g., Rocha-Pinto et al. 2000). Gas accretion may also control, in part, the evolution of the elemental abundances in galaxies and could also play a role in the mass–metallicity relationship (e.g., Kacprzak et al. 2016). These exchanges of matter through the CGM thus play critical roles in the evolution of galaxies. In our Cosmic Origins Spectrograph (COS) CGM Compendium (CCC) presented in this paper, we aim to directly explore how a specific property of the CGM—the metallicity—is distributed throughout cosmic time and environments.

Observationally, outflows have been characterized at various redshifts and appear ubiquitous in the universe (e.g., Shapley et al. 2003; Weiner et al. 2009; Steidel et al. 2010; Martin et al. 2013; Rubin et al. 2014). However, direct

observational evidence for cold gas accretion (colder than the virial temperature, i.e., gas at $\sim 10^4$ – 10^5 K) has been more difficult to discover. There is some evidence for gas accretion onto the Milky Way and other nearby galaxies (e.g., Wakker 2001; Fraternali & Binney 2008; Fox et al. 2016, 2018). Recent integral-field spectroscopic observations and studies of redshift-space distortions also suggest some evidence of inflows at low and high redshifts (e.g., Fumagalli et al. 2016; Bielby et al. 2017; Cantalupo 2017; Turner et al. 2017). The $z = 0$ observations indicate that gas can be accreted via means other than cold flow accretion, while the higher redshift results provide some support for cold flow accretion as observed in simulations, although none of these observational results show yet conclusively and unambiguously the existence of IGM gaseous filaments feeding galaxies. Another indirect way to probe cold flow accretion (and more generally gas flows in and out of galaxies) is via QSO absorbers that probe the CGM of galaxies. According to cosmological simulations (e.g., Fumagalli et al. 2011b; van de Voort & Schaye 2012; van de Voort et al. 2012; Faucher-Giguère et al. 2015; Hafen et al. 2017), the covering fraction of the cold streams in these simulations appears to peak in a H I column density (N_{HI}) regime known as the (partial) Lyman limit systems (pLLSs and LLSs). Using QSO spectra, we can search specifically for these absorbers and empirically characterize their properties.

In this and subsequent papers, we adhere to the following definition for the various absorbers studied in our survey. The pLLSs and LLSs have H I column densities $16.2 \lesssim \log N_{\text{HI}} < 17.2$ and $17.2 \leq \log N_{\text{HI}} < 19$, respectively. The $\log N_{\text{HI}} = 17.2$ cutoff corresponds to an optical depth at

the Lyman limit $\tau_{LL} = 1$ ($\tau_{LL} \equiv N_{H1}\sigma_{H1}$, where $\sigma_{H1} = 6.30 \times 10^{-18} \text{ cm}^2$ is the absorption cross section of a hydrogen atom at the Lyman limit, see Spitzer 1978). The 16.2 dex lower bound of the pLLSs is more arbitrary, but corresponds to $\tau_{LL} = 0.1$, which creates a break at the Lyman limit that is still visible in moderate and high signal-to-noise ratio (S/N) spectra (see Lehner et al. 2013, hereafter L13). This definition of LLSs differs from our previous surveys but follows more closely the generally adopted definition of LLSs and is motivated by the finding of Wotta et al. (2016) (hereafter W16), which shows a tentative difference in the metallicity distribution between the pLLSs and LLSs at $z \lesssim 1$ (see below). We also use the standard definition for the damped Ly α absorbers (DLAs) that have $\log N_{H1} \geq 20.3$ and super-LLSs (SLLSs, a.k.a. sub-DLAs) with N_{H1} in the range of $19.0 \leq \log N_{H1} < 20.3$. The absorbers with $15 \lesssim \log N_{H1} < 16.2$ have no proper definition and we simply define these absorbers as the strong Ly α forest systems (SLFSs). We, however, emphasize that the SLFSs are more related to the diffuse CGM than the IGM at $z < 1$. Indeed, several studies of the galaxy-absorber two-point cross-correlation function have shown significant clustering between galaxies and SLFSs while a weak or absent clustering signal for weaker N_{H1} absorbers (e.g., Lanzetta et al. 1995; Bowen et al. 2002; Penton et al. 2002; Chen et al. 2005; Prochaska et al. 2011a, 2011b; Tejos et al. 2014), pointing to a strong physical connection between SLFSs (and other stronger HI absorbers) and galaxies.

While the diffuse gas probed by SLFSs, pLLSs, and LLSs cannot be yet directly imaged, the properties of these absorbers can inform us on their origins and hence help us characterize the gas in the CGM of galaxies at low redshift. One of the key properties is the metallicity, since the enrichment levels of the gas help in differentiating between the plausible origins of the gas (Fumagalli et al. 2011b; Ribaldo et al. 2011; L13). For example, we can differentiate accretion from the IGM (that is metal-poor) from the more metal-rich gas produced by galaxies (which we emphasize can be outflowing or inflowing). Determining the metallicity distribution of the CGM gas also informs us about the fraction that has remained mostly untouched by the successive episodes of star formation in galaxies over billions of years.

While metallicity estimates nearly always require large ionization corrections in the $15 < \log N_{H1} < 19$ range, several independent studies have shown that such corrections can be well constrained by the broad range of ions despite an uncertain EUV ionizing background (Howk et al. 2009; L13; Crighton et al. 2013; Fumagalli et al. 2016; W16). The uncertainty in the ionizing background can lead to an absolute uncertainty in the metallicity of a factor 2–3 (Howk et al. 2009; W16; Fumagalli et al. 2016). Though it is not precision cosmology, it is accurate enough to separate low from high metallicities as well as enable a determination of the metallicity probability distribution function of these absorbers. We bear in mind that this error level on the metallicity of the absorbers is comparable to the magnitude of uncertainty on chemical abundances determined from emission lines in galaxy spectra (e.g., Berg et al. 2016). However, we also note that the uncertainties in the metallicities for a given ionizing background are also typically quite small (depending on the exact constraints provided by the available ions; see L13; Fumagalli et al. 2016).

Over the last few years, our team has led several surveys of the metallicities of the pLLSs and LLSs at $z \lesssim 1$ (Lehner et al. 2009; L13; Ribaldo et al. 2011; Tripp et al. 2011; W16) and $z \sim 2$ –4 (Lehner et al. 2016, and see also Cooper et al. 2015; Fumagalli et al. 2016; Glidden et al. 2016). One of our main findings has been the first evidence of widespread low metallicity gas in the pLLS and LLS regimes that is not observed in higher column density absorbers at similar redshifts. At $z \lesssim 1$ there is indeed a clear prevalence of very low metallicity pLLSs with $[X/H] \equiv \log N_X/N_H - \log X/H_\odot \lesssim -1.4$ (where X is an α -element such as Mg, O, or Si) with $43\% \pm 8\%$ of the pLLSs with these low metallicities, while $<10\%$ of the DLAs and SLLSs have $[X/H] < -1.4$ (where X is now a α -element, Zn, or Fe corrected for depletion or α /Fe enhancement) (W16). The pLLSs and LLSs therefore uniquely probe metal-poor gas in relatively dense (denser than the IGM probed by weak Ly α forest absorbers) environments in the universe at low and high redshift (L13; W16; Cooper et al. 2015; Fumagalli et al. 2016; Glidden et al. 2016; Lehner et al. 2016). Another major finding from these initial surveys was that the shape of the metallicity distribution of the pLLSs at $z \lesssim 1$ appears to be bimodal with an equal number of pLLSs below and above $[X/H] = -1$, a functional form only observed at $z < 1$ (at $z > 2$, the metallicity distribution appears to be unimodal for similar absorbers, see Lehner et al. 2016).

These empirical results provide the first strong evidence of widespread very low metallicity gas around $z \lesssim 1$ galaxies that may possibly accrete onto galaxies, although we emphasize that there is not yet any direct evidence that this gas is actually accreting. Our initial survey consisted of 28 absorbers (23 pLLSs and 5 LLSs) (L13). Our second survey doubled the size of our initial sample (44 pLLSs and 11 LLSs), confirming our initial results, and tentatively demonstrating a possible change in the shape of the metallicity distribution between the pLLSs and LLSs and a lower frequency of metal-poor LLSs compared to pLLSs (W16). Our surveys have increased by an order of magnitude the number of pLLSs and LLSs where the metallicities have been estimated at $z \lesssim 1$ compared to the status prior to the installation of the COS onboard the *Hubble Space Telescope* (HST) (see compilation by Lehner et al. 2009 and references therein). However, the sample of absorbers is still relatively small, especially when we treat the pLLSs and LLSs separately. Furthermore to effectively probe the level of the IGM/CGM enrichment requires that we not only increase the number of strong HI absorbers, but that we also target lower N_{H1} absorbers.

We were awarded a HST Legacy program to produce the largest survey to date of H I-selected absorbers at $z \lesssim 1$ using the spectra observed with the high-resolution mode (G130M and G160M gratings) of COS available at the Barbara A. Mikulski Archive for Space Telescopes (MAST). This archive is the richest database of UV QSO spectra with sufficient quality (spectral resolution and S/N) that can permit accurate estimations of the column densities of metal and H I transitions. As we detail in this paper, N_{H1} can be well determined by modeling the entire Lyman series (which is accessible for $z_{\text{em}} \gtrsim 0.2$ QSOs in the COS bandpass). The rest-frame UV, FUV, and EUV wavelengths covered by the COS spectra include a large number of metal lines with a wide range of strengths and ionization states, and additional NUV transitions (Mg II $\lambda\lambda 2796, 2803$, Fe II $\lambda\lambda 2382, 2600$)

can be observed from ground-based telescopes for the redshifts probed by our survey.

At $z \lesssim 1$, we note that any absorbers with $N_{\text{HI}} \gtrsim 10^{15.2} \text{ cm}^{-2}$ are in a relative “sweet spot” for an unbiased metallicity study because both the metal and HI column densities can be accurately estimated to provide a reliable census of the metallicity distribution. The S/Ns of the COS spectra are, however, not high enough to pursue an unbiased survey of the metallicity in the more diffuse gas probed by Ly α forest absorbers with $\log N_{\text{HI}} < 15$ at $z \lesssim 1$.

Here we present our CCC survey of HI-selected absorbers with column densities in the range of $15 < \log N_{\text{HI}} < 19$ at $z \lesssim 1$ aimed to determine the metallicities of these absorbers. We used the *HST* COS G130M and G160M archive that we supplemented with additional spectra of Mg II and Fe II NUV NUV obtained from the High Resolution Echelle Spectrometer (HIRES) on Keck I and the Ultraviolet and Visual Echelle Spectrograph (UVES) on the Very Large Telescope (VLT). Our COS G130M and G160M survey presented here comprises 224 absorbers, and our total sample for the metallicity study has 263 absorbers (the additional absorbers that were primarily observed with other instruments or gratings). In this paper, we present the design survey, observations, and data reductions (Section 2), the search for strong HI absorption in the COS spectra (Section 3) and column density and kinematics measurements of the 224 absorbers (Section 4), and the immediate implications from these measurements (Section 5). We summarize our main results in Section 6. In subsequent papers, we will present the grids of ionization models combined with a Bayesian formalism and Markov Chain Monte Carlo techniques to robustly determine the metallicities (and errors) of the absorbers (Wotta et al. 2018 paper II), the metallicity probability distribution of the pLLSs and LLSs (paper II) and SLFSs (paper III), and the properties of the high ions in these absorbers (paper IV).

2. Survey Design, Database, and Observations

2.1. Sample Selection Criteria

Our main goal for this survey is to estimate the metallicities of absorbers in the *HST* COS G130M and G160M archive. This requires that we select absorbers for which it is possible to derive the column densities of HI and at least some metal ions (preferably α elements like O, Mg, and Si). In order not to bias our survey toward low or high metallicities, this requires that (1) we identify absorbers based on their HI content alone, and (2) we must also be sensitive to metal-line absorption. Since the typical S/Ns of the COS G130M and G160M data are $\lesssim 30$ (and often $\lesssim 10$) per resolution element, we have determined—using guidance from Cloudy simulations—that this requires $\log N_{\text{HI}} \gtrsim 15.2$ at $z \lesssim 1$ to be sensitive to metallicities $[X/\text{H}] \lesssim -1$ (see also below).⁵ Therefore, our survey is HI-selected so that $\log N_{\text{HI}} \gtrsim 15.2$. In Section 3, we provide more details on the search for the absorbers.

We note that a more subtle bias could, in principle, be introduced into our survey if a large number of absorbers were initially targeted because they were known a priori to be metal-rich or poor systems. To the best of our knowledge and after

scanning through the description of the various *HST* programs that originally obtained the data, we feel that our survey is not adversely affected in this way; i.e., most of the absorbers were serendipitously observed in the spectra that targeted other science goals (e.g., study of the Milky Way halo, Local Group gas, and the diffuse IGM). The only exception that we are aware of is the metal-poor absorber at $z = 0.660356$ toward J131956.23+272808.2 (a.k.a, CSO-0873 or TON153), which was selected based on its Mg II absorption (Churchill et al. 2012; Kacprzak et al. 2012), as already noted in L13. Here we provide a new estimate of its HI column density, but do not include this absorber in our survey. Several absorbers were also found in the spectra from the COS-Halos survey (Tumlinson et al. 2011, 2013; Werk et al. 2013, 2014), but the vast majority of those are not the absorbers that were initially targeted to probe the CGM of their galaxy sample. In fact we have only nine absorbers in common with the targeted COS-Halos absorbers. This number is not larger because (1) several of the COS-Halos absorbers have either lower or higher N_{HI} than probed by our survey; (2) several of the COS-Halos absorbers have $z_{\text{abs}} < 0.2$, which is outside our redshift search range (see Section 3); (3) we did not use the subsequent COS G140L spectra obtained by the COS-Halos team to determine N_{HI} for absorbers that had only a lower limit on N_{HI} from the G130M and G160M spectra; and (4) for a couple of absorbers we could not derive a reliable N_{HI} . We will provide a detailed comparison of our results with those from COS-Halos in paper III.

We note that our identification and analysis of absorbers, including estimations of their metallicities, is somewhat different than that adopted by COS-Halos and by several other surveys of high column density absorbers. Where possible, we separate individual absorbers on the basis of our ability to cleanly resolve them from one another in the *HST*/COS spectroscopy. We do not impose a minimum velocity or redshift window across which we assume all absorption is associated with a single system. This is related to the discussion above, in that we only associate metal-line absorption with its directly associated HI absorption component. We note that this choice amounts to a different working definition of what constitutes an absorption system. As we discuss in Section 5.5, absorbers closely separated in redshift space ($\Delta v \leq 500 \text{ km s}^{-1}$) consist only of about 13% of the sample analyzed in this paper.

In our search, we also did not reject a priori proximate absorbers, i.e., absorbers spatially close in redshift space to the background QSO (in this work defined as $\Delta v < 3000 \text{ km s}^{-1}$). The proximate absorbers constitute a small fraction of the sample with only 5% of the absorbers being proximate (see Section 5.5). In papers II and III, we will note the influence of these proximate absorbers on our results as needed, but they represent a small portion of the sample, and we will demonstrate they have little impact on the overall properties we derive from our survey.

2.2. COS Data and Database

Our survey makes use of the extended archival UV spectroscopy of AGN and QSOs taken with the highest-resolution modes of the COS instrument. General information on the design and performance of COS can be found in Green et al. (2012). We used only data taken with the COS G130M and G160M gratings, with spectral resolutions $R \approx 17,000$

⁵ As we detail below, we can also use the Mg II $\lambda\lambda 2796, 2803$ doublet obtained from ground-based telescopes to derive the metallicity, but for $\log N_{\text{HI}} \gtrsim 15.2$, it becomes prohibitively expensive, since it requires S/N $\gtrsim 100$ in the high-resolution mode of a 8–10 m telescope.

(or about $15\text{--}20\text{ km s}^{-1}$). All the COS G130M and G160M data were retrieved from MAST. Our work started prior to the release of the *HST* Spectroscopic Legacy Archive (HSLA, Peebles et al. 2017) reduction of the COS archival data. Thus, we searched the MAST archive for observations of AGN/QSOs taken with the G130M and/or G160M observations using a set of “Target Description” keywords possibly related to such observations.⁶ Our first search of the archive was completed on 2014 August 28, and resulted in a list of 480 candidate objects. We then used a SIMBAD search on the basis of the target coordinates to determine the type and redshift of these objects. Our initial selection of keywords yielded 96% of AGNs/QSOs at $z < 1.5$. The remaining objects consisted of higher redshift QSOs and a handful of stars from the Magellanic Clouds.

We performed a follow-up search on 2016 April 20, which yielded a database of 527 objects, adding only 47 objects in the nearly 20-month span between the two searches. Removing stars and high-redshift QSOs, our final database consists of 507 targets at $z < 1.5$. We cross-correlated our database with HSLA when it was released and found the same list of objects. Although we adopted the HSLA spectra (but see Section 2.3.2 for some exceptions), we kept our original database information and structure for our survey.

2.3. Data Reduction and Coaddition

As we were finalizing our search for strong H I-selected absorbers (Section 3), the HSLA became available, which provided coadded spectra across different programs of the same object. Since the HSLA data are likely to become the reference spectral database in the UV and since the data quality are equivalent to our initial database (see below), we decided to adopt the spectra from the HSLA for our survey. This is also beneficial for the reproducibility of our results. Furthermore, the HSLA handles the errors properly, with a coaddition of the data in counts rather than flux that allows for a cleaner propagation of the photometric error (Gehrels 1986). However, one of the limitations of the HSLA spectra is that they were obtained with no attempt to shift different exposures relative to one another to correct for any possible mismatch in the wavelength calibration. This can lead to blurred absorption line profiles, which could adversely affect our results. Since we did our own coaddition of the QSO spectra prior to the availability of the HSLA, we discuss below the cross-comparison between our original database and the HSLA after describing our coaddition procedure.

2.3.1. Original Coaddition

We used data reduced with the standard *calcos* pipeline at MAST. While the *calcos* pipeline provides a coaddition of the different exposures for a given program (without any cross-correlation of absorption lines), it does not coadd data across different programs or observed with different grating settings. In order to get the best S/N spectra, we needed to coadd data and we used the updated *coadd_x1d* algorithm from the COS GTO team (see Danforth et al. 2016; Keeney et al. 2017) to coadd the COS G130M and G160M spectra. We chose this algorithm because it maintains an appropriate flux calibration for the resulting spectra (critical for modeling the break at the

Lyman limit if in existence, see Section 4.3), is fully automated, and has the possibility to coadd various settings straightforwardly. In view of the large sample that we analyzed, it was critical that little human interaction was required to produce the final data sets.

This coadding program cross-correlates strong absorption lines to add the different exposures obtained from the same or different settings (different central wavelengths or gratings). More details can be found in Danforth et al. (2016). The main caveat with this program is, however, that it does not handle the COS wavelength stretches that have been described in, e.g., Wakker et al. (2015), where misalignments of a few tens of km s^{-1} that vary as a function of wavelength can occur between different exposures.

We tested the results from this coaddition with other coadditions that we undertook for our first survey (L13) and our M31 halo survey (Lehner et al. 2015) where the individual exposures were coadded by two different algorithms. For the column densities, we systematically obtain comparable results for both the actual values of the column densities and the errors. The coadding program developed by Wakker et al. (2015) cross-correlates each line in each exposure over a small wavelength range to account for the COS wavelength stretches, providing currently the best wavelength calibration solution; this program was adopted for the M31 survey because accurate absolute velocities were critical. So, while the derived column densities agree typically within 1σ error, there were a few cases where the absolute velocities between the two reductions could differ by one or two COS resolution elements (i.e., $15\text{--}30\text{ km s}^{-1}$). As accurate velocities/redshifts are not too critical for the main aim of our survey (but see Section 2.4), the fully automated *coadd_x1d* program provided coadded COS spectra of adequate quality.

2.3.2. Comparison with HSLA

We first visually compared our own and the HSLA coadditions, and overall the spectra look equivalent with a similar S/N, except sometimes in the G130M/G160M overlap region where the HSLA sometimes fails to correctly coadd the data. This can lead to an artificial break in the flux or a much lower S/N in that region of the final spectrum (see in the current HSLA data release, e.g., the spectra of PHL2525, 3C263, or MRK421). Generally, the overlap region between the two gratings was not critical for our work (i.e., in most cases no key absorption features or LLS breaks fell in that region). In cases where several transitions fell in that overlapping region, we adopted our initial coaddition (e.g., the absorber $z=0.556684$ toward J124511.25+335610.1 is such an example where several critical H I transitions were present in that overlap region).

Using the coadded spectra from our original database and the HSLA, we compared the normalized spectra for several absorbers as well as estimated column densities and kinematics. We found consistent results within less than 1σ (and, importantly, comparable errors). In particular, as detailed below, we re-analyzed several COS absorbers from the L13 sample and overall we derived column densities in agreement within about 1σ .

Therefore, despite the inconvenience for a few absorbers where the absorption feature fell in the G130M/G160M overlap region and because overall the HSLA and our coadded spectra gave consistent results, we decided to adopt the HSLA

⁶ This was a somewhat cumbersome process, as the Target Descriptions are chosen by the individual PIs and have no checks or requirements for accuracy.

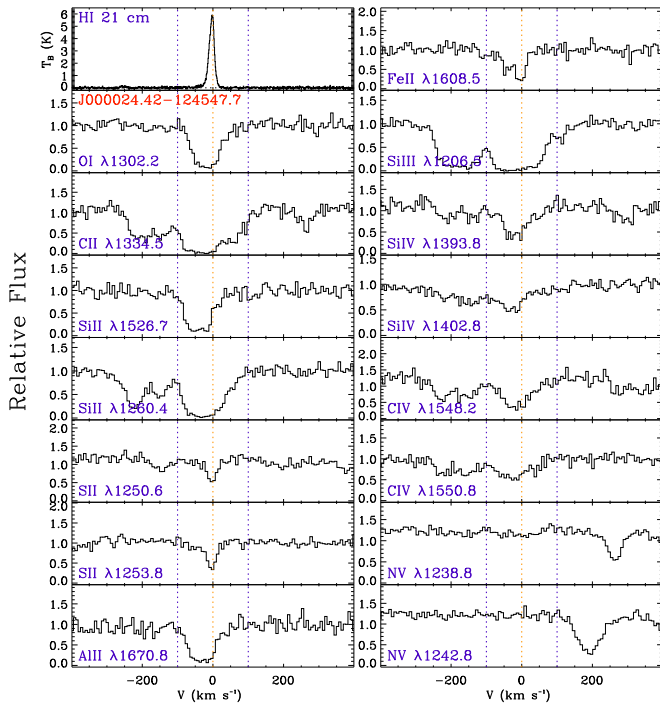


Figure 1. Velocity profiles for key atoms and ions for which the absorption arises from the Milky Way compared to the H I emission (top-left panel) of the Milky Way toward the same direction. The vertical dotted lines just show -100 , 0 , and 100 km s^{-1} for reference. This type of figure was produced for each object in our database to help determine if there were any issues with the COS wavelength calibration.

data. For ease of manipulating our database and plotting figures, we, however, enhanced the original FITS files provided by the HSLA by adding several keywords, including the redshift of the objects, the right ascension, declination, Galactic longitude and latitude, the *HST* and SIMBAD names, the minimum and maximum wavelengths, and the conversion needed to shift velocities to the Local Standard of Rest (useful, e.g., for aligning Milky Way absorption with H I 21 cm emission profiles).

2.4. COS Wavelength Calibration

As we already discussed in Section 2.3.1, there are known issues in the COS wavelength calibration, both in the absolute and relative wavelength calibrations. For the data used in our survey, we find that these effects are typically less than $20\text{--}30 \text{ km s}^{-1}$ as we now demonstrate.

First, for all the 527 objects that were in our initial database, we visually compared the absorption seen in the atomic and ionic transitions from the Milky Way and the Galactic H I 21 cm emission from the Leiden/Argentine/Bonn (LAB) Survey (Kalberla et al. 2005) observed in the same direction. As the H I emission velocity is well calibrated, this comparison helps in assessing the overall accuracy of the absolute wavelength calibration as well as possible relative shifts between different transitions if they originate from the same gas. In Figure 1, we show an example of a figure that we produced for all the objects in our database where we display a stack of velocity profiles of several atomic and ionic COS transitions and the H I emission from the LAB data. Since H I emission is probing the neutral gas, the best species to compare with is O I or N I, but these are often affected by strong airglow emission lines and strongly saturated.

We therefore used singly ionized species and also used higher ions (Si III, Si IV, C IV, and N V) to assess possible velocity differences between the ionized and neutral gas. In addition, we consider several transitions of each ion where possible because some Milky Way absorption features can be contaminated by IGM or CGM absorption at higher redshifts. The velocity profiles shown in Figure 1 illustrate some of the issues. The saturated transitions of singly ionized species appear somewhat shifted relative to the main H I emission, but they appear to be aligned with strong lines from doubly and triply ionized species. This is largely due to the strong saturation across several of the components in the low-velocity gas, as the velocity of the absorption in the weaker transitions of singly ionized species (e.g., S II $\lambda 1253$ and Fe II $\lambda 1608$) matches well the velocity of the main H I emission. Hence for this target, we conclude that the absolute COS wavelength calibration is good to within one COS resolution element. We considered the calibration for our entire database in this way. We typically found comparable results, with absolute wavelength calibrations good to $\sim 20\text{--}30 \text{ km s}^{-1}$. A notable exception in our survey is J154553.63+093620.5 where the absorption was shifted by -50 km s^{-1} , which we subsequently corrected.

Second, several targets were observed with ground-based telescopes to obtain Mg II $\lambda 2796$, 2803 (see Section 2.6). In that case, we can again test the relative and absolute wavelength calibration, but this time using the observed species at the redshift of the absorber. We found again that the velocity of Mg II (when detected) was typically aligned with the COS transitions in the redshifted rest frame of the absorber. The main exception was again J154553.63+093620.5 where a similar velocity shift determined with the previous method was derived.

Third, we fitted the H I Lyman series with Voigt profiles for a large fraction of our sample. That is the only part in our survey where an alignment is critical to obtain the best possible fit. As we discuss in more detail in Section 4.3, overall we found a good match between the central velocities of the different H I transitions, suggesting the relative wavelength calibration was secure (to the limits we need) across at least the wavelengths probed by the Lyman series absorption. Only in a few rare cases did we need to shift a specific H I transition to match the velocities of the other H I lines in order to have a better-fitted profile (this was automatically taken care of in the profile fitting (PF), see Section 4.3).

2.5. Adopted Database

While our initial database had 527 QSO spectra, the final sample for our survey was reduced to 335 QSOs based on quality cuts to those observations and selection criteria of our targets. Deriving accurate $N_{\text{H I}}$ for absorbers with $\log N_{\text{H I}} \gtrsim 15.2$ requires (1) observability of several Lyman series transitions beyond Ly α and Ly β (i.e., $z_{\text{em}} \gtrsim 0.17$ to redshift the Lyman series in the COS wavelength) and (2) $S/N \gtrsim 1$ in the COS spectra with a bin size of $\sim 6 \text{ km s}^{-1}$ (or $S/N \gtrsim 2$ per resolution element—hereafter any S/N value is for a COS spectrum with 6 km s^{-1} bin size; we searched for absorbers in even lower S/N spectra, but none were reliably found; see Section 3 for more details).⁷

⁷ Ultimately all the QSO spectra with absorbers included in our H I-selected survey have a $S/N \gtrsim 2.5$ (there are 294 QSOs satisfying this S/N threshold). In the 41 QSO spectra with $1 < S/N < 2.5$, we found only two very strong H I absorbers for which we could derive only a lower limit on $N_{\text{H I}}$.

Table 1
Sample of Targets

Name	<i>HST</i> Name	z_{em}	λ_{min} (Å)	λ_{max} (Å)	S/N	PID	N_{abs}	Obs.
J000024.42-124547.7	PHL2525	0.20000	1132.6	1760.0	18.0	12604	0	...
J000559.23+160948.9	PG0003+158	0.45045	1132.7	1792.2	24.2	12038	3	UVES
J001224.02-102226.3	SDSSJ001224.01-102226.5	0.22822	1135.4	1795.5	5.4	12248	0	...
J002330.58+154744.9	J002330.58+154744.9	0.41041	1144.0	1460.5	4.6	14071	0	...
J004222.29-103743.8	SDSSJ004222.29-103743.8	0.42397	1135.5	1795.5	6.5	11598	1	HIRES

Note. Each of these targets was observed with COS G130M and/or G160M. S/N is given in for COS spectra binned by 3 pixels per resolution element. N_{abs} is the number of absorbers along a given sightline where we could estimate reliable column densities and metallicities. If a number is between parentheses in the column N_{abs} , it means we could only derive a lower limit on $N_{\text{H I}}$, except for J131956.23+272808.2 where the absorber at $z = 0.660356$ was originally selected based on the presence of Mg II (see text for more details); in all these cases, these absorbers are not included further in our H I-selected survey.

(This table is available in its entirety in machine-readable form.)

In Table 1, we summarize the QSO sample over which we carried out our search for strong H I absorption, sorted by increasing right ascension. The first column gives the J2000 name, constructed using the right ascension and declination in J2000 sexagesimal format (JHHMMSS.ss+DDMMSS.s; note that the output is truncated in precision rather than rounded following the IAU recommendation and the official SDSS designation). The second column gives the PI-provided name from the *HST* observations, i.e., the name as displayed in MAST. We provide that information to simplify the search in the MAST archive (many of the “*HST* names” are not standard and thus will not be resolvable in SIMBAD). The third column gives the redshifts that we extracted from SIMBAD (overall these are equivalent to those listed in the HSLA that come from the NASA/IPAC Extragalactic Database). The next three columns give the wavelength coverage and median S/N of the COS spectra. Spectra with $\lambda_{\text{max}} \lesssim 1480$ Å were obtained with the COS G130M grating setting only; spectra with $\lambda_{\text{min}} \gtrsim 1400$ Å were obtained with the G160M grating setting only; spectra that cover wavelengths from ~ 1130 – 1800 Å were obtained with both COS G130M and G160M gratings. The seventh column provides the *HST* program identification number of the original program(s) used for each target. The eighth column provides information regarding the number of absorbers with $\log N_{\text{H I}} > 15.1$ found in a given spectrum; a number between parenthesis means that a strong H I absorber with $\log N_{\text{H I}} \gtrsim 17.9$ was found but we were not able to constrain $N_{\text{H I}}$ better than a lower limit. Finally, the last column provides information if supplemental ground-based spectra exist with the name of the instrument used. These ground-based spectra cover, in particular, the strong Mg II $\lambda\lambda 2796, 2803$ doublet discussed below.

2.6. Supporting Ground-based Observations

Our survey includes new and archival spectroscopy obtained with ground-based instruments. As demonstrated in L13 and W16, the Mg II $\lambda\lambda 2796, 2803$ doublet is an excellent metallicity tracer for pLLSs and LLSs (and as we will show in paper III, even for the weaker absorbers with $15.2 \lesssim \log N_{\text{H I}} \lesssim 16.1$) because it is so strong. A large fraction of the ground-based observations also covers the strong transitions of Fe II $\lambda\lambda 2382, 2600$ (depending on the redshift of the absorbers and wavelength coverage in the blue), providing additional information on nucleosynthesis and depletion effects (which are mild; see L13 and Section 5.4).

The two main ground-based telescopes and instruments used in our survey are the HIRES, Vogt et al. 1994) on Keck I and the UVES on the VLT (Dekker et al. 2000). For one of the absorbers we also used low-resolution spectra from SDSS and for another one the Multi-object Double Spectrograph (MODS) on the Large Binocular Telescope (LBT); we note that the absorption for these two absorbers is very strong and only lower limits could be derived on the column densities of Mg II. For the LBT/MODS data processing, we refer the reader to W16.

For the UVES data, archival data were used for four sightlines, retrieved from the ESO archive. Another 12 targets were observed through our ESO VLT/UVES program 0100. A-0483, which was awarded up to 31 hr of VLT/UVES “filler” time during period 100A (data were acquired from 2017 September to 2018 March). This program used a 1” slit with Dichroic #1 to obtain $R \sim 40,000$ data target Mg II absorption from CGM absorbers. For sightlines with systems below $z \lesssim 0.25$, we used the 346 + 564 grating setting to provide coverage over the wavelength ranges of $3200 \lesssim \lambda \lesssim 3900$ and $4700 \lesssim \lambda \lesssim 6600$ Å. For all others we used the 390 + 564 setting, producing usable data over roughly $3300 \lesssim \lambda \lesssim 6600$ Å. The nominal exposure times were designed to achieve $S/N \gtrsim 10$ per pixel for Mg II at the lowest-redshift absorber along a sightline. Our observations were taken over a wide range of conditions, and not all observing setups for a given target were necessarily executed. Thus, the S/N achieved varies between targets (as well as with wavelength for a given target). To reduce the UVES spectra (archival and new data), we use the ESO pipeline data reductions, which is adequate for the data quality that we obtained.

The bulk of our ground-based observations come from Keck HIRES observation. In total 53 sightlines in our sample were observed with Keck HIRES. About 75% of this sample comes from the KODIAQ (Keck Observatory Database of Ionized Absorbers toward QSOs) database available at the Keck Observatory Archive (KOA) (Lehner et al. 2014; O’Meara et al. 2015, 2017). KODIAQ consists of a uniformly and fully reduced sample of QSOs by our group at $0.07 < z_{\text{em}} < 5.29$ observed with Keck HIRES at high resolution. Most of the spectra for QSOs with $z \lesssim 1.3$ in the KODIAQ database were initially obtained to support two Large *HST* programs, COS-Halos and the COS Absorption Survey of Baryon Harbors (Tripp et al. 2011; Tumlinson et al. 2011). The remaining 25% was obtained through the NASA and University of Hawai’i at

Hilo Keck allocation time (PIs: O’Meara and Cooksey, respectively). We applied the same data reduction to these data that was applied to the KODIAQ sample (O’Meara et al. 2015), and these spectra will be included in the next KODIAQ data release.

In total, there are 64 high-resolution HIRES and UVES QSO spectra that have a coverage of 113 absorbers (see Table 1 for the listing of sightlines observed from the ground). The absorbers toward J113327.78+032719.1 and J213135.20-120704.5, observed with HIRES and UVES, respectively, both had very strong absorbers with $\log N_{\text{H I}} \gtrsim 18$; as only a lower limit could be derived on the $N_{\text{H I}}$, these two absorbers are not included in our final sample for studying metallicities. In Section 5.3, we provide more information regarding the sensitivity of the ground-based observations, but our general aim was to obtain spectra with S/Ns that gave $W_\lambda \lesssim 25$ mÅ at the 2σ level (over a typical integration range of ± 15 km s $^{-1}$ or a full velocity width of about 30 km s $^{-1}$). This sensitivity level is critical to placing robust limits on low-metallicity gas.

3. Search for Strong H I-selected Absorbers

Our survey is based on a search of the entire database of COS G130M and/or G160M spectra for absorbers with $\log N_{\text{H I}} \gtrsim 15.2$. Absorbers with $\log N_{\text{H I}} \gtrsim 16.5$ create a strong enough break at the Lyman limit in the continuum of the QSO so that a visual inspection of the spectra allows one to identify these absorbers readily, even in low S/N spectra.⁸ However, for lower $N_{\text{H I}}$ absorbers, the signature of the Lyman break and even the convergence of the Lyman series near the Lyman limit are not readily observable or more difficult to discern.

We therefore developed and used an automated search tool for identifying strong H I absorption. The initial step in the search was to fit a continuum to the entire spectrum of a given QSO. While this large-scale continuum is not adequate for quantitative measurements of the absorption lines, it is good enough to allow a search for strong H I Lyman series lines. To enable this continuum fit, we first masked all the relatively strong absorption features observed in the QSO spectrum. The continuum estimate was then a heavily rebinned version of the input spectrum after masking. We interpolated across the masked regions, assuming little variation in the continuum level over these masked regions. Since abrupt changes in the continuum slope can be observed near the peak of the emission lines, we allowed for a refined binning over such regions. An example of the final continuum model is shown in Figure 2, which demonstrates that this approach provides a continuum model good enough to enable a search for specific absorption features in the spectrum. We emphasize that we did not use this continuum model to make quantitative measurements of the absorption lines.

We identified strong H I absorption systems based on the presence of Lyman series transitions from 1215.7 Å (Ly α) down to 937.8 Å (Ly ϵ). Absorbers with $\log N_{\text{H I}} \gtrsim 15.2$ should produce visible absorption down to at least Ly ϵ , and we used this as a criterion for identification of such absorbers. At the resolution of COS G130M and G160M data, H I absorbers in our target range always show saturated absorption in Ly α and Ly β . We therefore also required that if Ly α and/or Ly β are

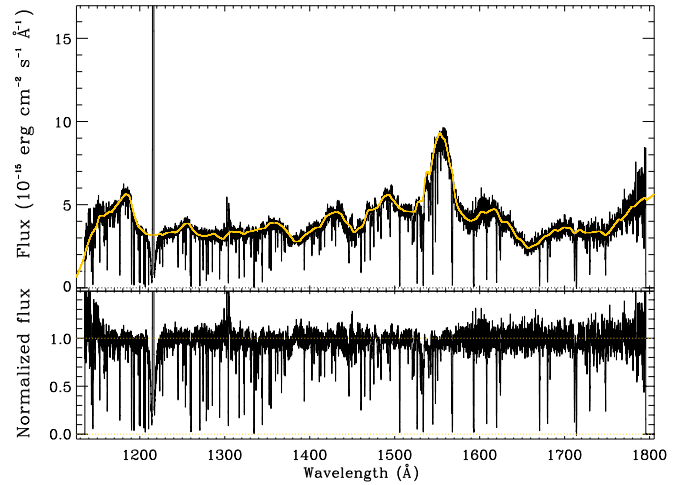


Figure 2. Example of a continuum fit on the entire observed spectrum (top) and resulting normalized spectrum (bottom) for the QSO J110539.79+342534.3 at $z_{\text{em}} = 0.50901$. This continuum was solely used for the automated search of strong H I absorbers in each QSO spectrum in our database.

covered for a candidate absorber, at minimum three contiguous pixels in the cores of these lines reach a value at or below 0.5 times the flux value corresponding to the 1σ error on the flux. These search criteria are insensitive to the broadening of the absorbers as long as the Doppler parameter $b \lesssim 80$ km s $^{-1}$. Using our PF code (see Section 4.3), we generated absorption profiles convolved with the COS G130M and G160M line-spread functions for an absorber with $\log N_{\text{H I}} = 15.3$ from Ly α to Ly ϵ where b was allowed to vary from 20–80 km s $^{-1}$ and overplotted these profiles on a COS G130M and G160M spectrum with S/N $\simeq 5$, showing that even if $b = 80$ km s $^{-1}$, absorption would still be detected in H I $\lambda\lambda 937.7, 949.7$ transitions and the profiles of Ly α and Ly β would be strongly saturated.⁹ We are therefore confident that our search algorithm did not miss broad H I absorbers with $\log N_{\text{H I}} \gtrsim 15.2$. As we will show in Section 5.2 there is no evidence of absorbers with $b > 50$ km s $^{-1}$ and $\log N_{\text{H I}} \gtrsim 15.2$ at $z \lesssim 1$, consistent with the smaller but higher resolution survey by Lehner et al. (2007).

Our program computed the wavelength path to search based on the combination of the maximum and minimum observed wavelengths and redshift of the QSO. Since we require access to transitions weaker than Ly γ to derive accurate $N_{\text{H I}}$ values, the lowest redshift in our survey when G130M data are available is $z_{\text{min}} \sim 0.2$. The maximum redshift accessible with the G160M data is $z_{\text{max}} \sim 0.9$. Our search program scanned each QSO spectrum starting from the highest redshift available (either observable or the QSO redshift); checked for the existence of Lyman series absorption from Ly α to Ly ϵ (if Ly α is outside the wavelength range, it adopted Ly β or Ly γ , etc.); and, if the Ly α or Ly β transitions are covered, it ensured that several contiguous pixels in the line centers were saturated (see above), helping to reduce the number of false-positive candidates. If all these conditions were satisfied, the program produced a stack of normalized profiles against the rest-frame velocity from Ly α to Ly-11 $\lambda 918.12$ at the identified redshift of the absorber. The program then iterated to search for additional

⁸ In the higher S/N spectrum (such as those analyzed in the L13 sample), a break can be observed down to $\log N_{\text{H I}} \gtrsim 16.2$, which was the H I column density limit in L13.

⁹ We did not consider broader components since Lehner et al. (2007) show these are quite rare and are only seen for H I absorbers with $\log N_{\text{H I}} \lesssim 13.4$. In fact, we note that according to their high-resolution (*HST*/STIS E140M) survey, the eight absorbers with $\log N_{\text{H I}} \gtrsim 15.1$ all have $b \lesssim 50$ km s $^{-1}$ in their survey (see Figure 5 in Lehner et al. 2007).

Table 2
Atomic Parameters and Abundances for the Surveyed Atoms and Ions

Species	λ (Å)	$\log \lambda f$	A_{\odot}	Ion. Flg.
H I	1215.6700	2.70	12.00	1
H I	1025.7222	1.91	12.00	1
H I	972.5367	1.45	12.00	1
H I	949.7430	1.12	12.00	1
H I	937.8034	0.86	12.00	1
H I	930.7482	0.65	12.00	1
H I	926.2256	0.47	12.00	1
H I	923.1503	0.31	12.00	1
H I	920.9630	0.17	12.00	1
H I	919.3513	0.04	12.00	1
H I	916.4291	-0.28	12.00	1
H I	917.1805	-0.18	12.00	1
H I	918.1293	-0.07	12.00	1
H I	915.3289	-0.45	12.00	1
H I	914.9192	-0.53	12.00	1
H I	914.5762	-0.61	12.00	1
O I	1302.1685	1.80	8.69	1
O I	988.7734	1.66	8.69	1
O I	1039.2304	0.97	8.69	1
O II	834.4650	2.04	8.69	1
O II	833.3294	1.87	8.69	1
O II	832.7572	1.57	8.69	1
O III	702.3320	1.98	8.69	4
O III	832.9270	1.95	8.69	4
O IV	787.7110	1.94	8.69	5
O IV	608.3980	1.61	8.69	5
O V	629.7300	2.51	8.69	5
O VI	1031.9261	2.14	8.69	5
O VI	1037.6167	1.83	8.69	5
C II	903.9616	2.48	8.43	2
C II	1334.5323	2.23	8.43	2
C II	903.6235	2.18	8.43	2
C II	1036.3367	2.09	8.43	2
C III	977.0201	2.87	8.43	2
C IV	1548.2040	2.47	8.43	5
C IV	1550.7810	2.17	8.43	5
Ne VIII	770.4090	1.90	7.93	5
Ne VIII	780.3240	1.60	7.93	5
Mg II	2796.3543	3.24	7.53	1
Mg II	2803.5315	2.93	7.53	1
Mg X	609.7900	1.71	7.53	5
Mg X	624.9500	1.41	7.53	5
N I	1199.5496	2.20	7.83	3
N I	1200.2233	2.02	7.83	3
N I	1200.7098	1.71	7.83	3
N I	1134.9803	1.67	7.83	3
N I	1134.4149	1.51	7.83	3
N I	1134.1653	1.22	7.83	3
N II	1083.9937	2.08	7.83	3
N III	989.7990	2.09	7.83	3
N III	763.3400	1.80	7.83	3
N IV	765.1480	2.67	7.83	5
N V	1238.8210	2.29	7.83	5
N V	1242.8040	1.98	7.83	5
Si II	1260.4221	3.17	7.51	1
Si II	1193.2897	2.84	7.51	1
Si II	1190.4158	2.54	7.51	1
Si II	1526.7070	2.31	7.51	1
Si II	1304.3702	2.05	7.51	1
Si II	1020.6989	1.23	7.51	1
Si III	1206.5000	3.29	7.51	1
Si IV	1393.7602	2.85	7.51	4
Si IV	1402.7729	2.55	7.51	4

Table 2
(Continued)

Species	λ (Å)	$\log \lambda f$	A_{\odot}	Ion. Flg.
Fe II	2600.1729	2.79	7.45	3
Fe II	2382.7652	2.88	7.45	3
Fe II	1144.9379	1.98	7.45	3
Fe II	1608.4511	1.97	7.45	3
Fe III	1122.5240	1.79	7.45	3
S II	1259.5180	1.32	7.14	1
S II	1253.8050	1.14	7.14	1
S II	1250.5780	0.83	7.14	1
S III	677.7460	3.05	7.14	1
S III	698.7310	2.74	7.14	1
S III	724.2890	2.41	7.14	1
S III	681.4700	1.67	7.14	1
S III	1012.4950	1.65	7.14	1
S III	1190.2030	1.45	7.14	1
S IV	657.3400	2.89	7.14	5
S IV	748.4000	2.57	7.14	5
S IV	744.9070	2.27	7.14	5
S IV	809.6680	1.93	7.14	5
S IV	1062.6640	1.72	7.14	5
S V	786.4800	3.05	7.14	5
S VI	933.3780	2.61	7.14	5
S VI	944.5230	2.31	7.14	5

Note. H I and metal ions and atoms that were systematically surveyed. Solar abundances are from Asplund et al. (2009). Atomic parameters for the FUV and EUV lines are from Morton (2003) and Verner et al. (1994), respectively. The table is sorted in decreasing order of abundances. The last column present the “ionization flag,” i.e., the elements that were used or not in the photoionization models in papers II and III: (1) these are α -elements with low ionization stages that are always used if uncontaminated; (2) always used if uncontaminated but allowing for possible variation in the $[C/\alpha]$ ratio; (3) often used, but sometimes removed because nucleosynthesis or depletion can affect the N/α or Fe/α ratio, respectively; (4) sometimes used depending on the ionization conditions as these ions can be produced by multiple ionization processes; and (5) never included because their ionization stages are too high to typically be produced by the same processes or at the same densities than observed for lower ions and H I.

(This table is available in machine-readable form.)

potential H I absorber(s) in a given QSO spectrum. Each stack of velocity profiles was then visually inspected to eliminate any residual false-positive absorbers (e.g., absorbers with $\log N_{\text{H I}} \lesssim 15$). To facilitate this examination, three H I models (convolved with the COS LSF) were overplotted for each transition showing the absorption expected for $\log N_{\text{H I}} = 15, 16$, and 17 and $b = 30 \text{ km s}^{-1}$.

We also independently performed a visual search for the signature of a break (or multiple breaks) caused by Lyman limit absorption in each QSO spectrum and determined the redshift of those using the Lyman series lines. The two searches led to the same identification of the strong systems with $\log N_{\text{H I}} \gtrsim 16.5$, with the following exception: where the automatic search program failed to identify an absorber that was identified visually, it was because the Lyman series transitions above 937 Å were not covered. None of these absorbers ended up in our sample because we could not reliably determine $N_{\text{H I}}$ for any of these absorbers (i.e., the Lyman limit break was saturated with no flux recovery).

Two recent surveys were undertaken with a smaller sample of COS spectra by Stevans et al. (2014) and Shull et al. (2017). We emphasize that we did not use their results for our survey (neither their column densities, nor their identification of the absorbers), and thus they serve as a good check on our search methodology. We compared the results of our survey with the absorbers with $\log N_{\text{HI}} \gtrsim 16$ reported in Shull et al. (2017) in their Table 6. All of the systems found by Shull et al. were identified in our search. The survey conducted by Stevans et al. (2014) included absorbers with $\log N_{\text{HI}} \gtrsim 13.4$. We compared the results for a few sightlines. Our search identified all of their absorbers meeting our selection criteria (redshift $z_{\text{abs}} \lesssim 0.9$ and $\log N_{\text{HI}} \gtrsim 15.2$), but absorbers for which N_{HI} could not be accurately estimated (to better than ~ 0.3 dex in $\log N_{\text{HI}}$) did not make it into our final sample.

The redshift of each absorber was determined from the peak optical depth of the strongest H I component in the automatic search process. In a few cases, this process was affected by contamination from other lines. In these cases, we adjusted the redshifts if they were offset by more than ~ 1 COS G130M–G160M resolution element ($\sim \pm 15 \text{ km s}^{-1}$). When they are detected, we found that low metal ions such as C II, O II, and Mg II are at the same redshifts as the strongest H I absorption component for a given absorber (within the COS velocity error of about 15 km s^{-1}).

4. Estimation of the Column Densities

Our automated search provided a sample of 224 absorbers. For each of the absorbers, we estimated column densities for all covered (and uncontaminated) transitions given in Table 2, amounting to column density estimates for several thousands of absorption lines. We developed a semi-automated approach to measuring these column densities in order to expedite and systematize the process. For each transition, an automated continuum was estimated as described in Section 4.1. Once the continuum placement was set, we employed the apparent optical depth (AOD) method (Savage & Sembach 1991) as described in Section 4.2 to estimate the total ionic or atomic column density. For H I, we used a combination of different methods as described in Section 4.3, depending in part on the strength of the absorption. Throughout we assumed the atomic parameters for the UV and EUV lines listed in Morton (2003) and Verner et al. (1994), respectively, including central wavelengths and f -values.

4.1. Continuum Modeling

To determine the line properties (equivalent widths, column densities, and velocities), we automatically fit the continuum near the absorption features using Legendre polynomials. A velocity region of about $\pm 2000 \text{ km s}^{-1}$ around the relevant absorption transition was initially considered for the continuum fit. This velocity interval could vary as described below, depending on the complexity of the spectrum (e.g., a region of a spectrum with a high density of absorption lines or with QSO emission lines). In all cases the interval for continuum fitting was never larger than $\pm 2000 \text{ km s}^{-1}$ or smaller than $\pm 250 \text{ km s}^{-1}$. Within this predefined region, the spectrum was broken into smaller sub-sections and then rebinned. The continuum was fit to all pixels that did not deviate by more than 2σ from the median flux in their local subsection. This removes pixels from the fitting process that may be associated

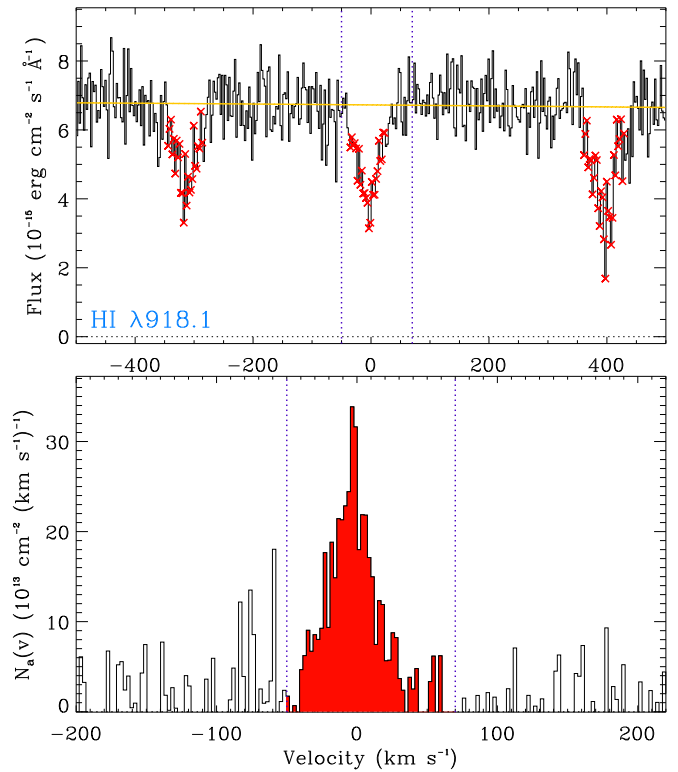


Figure 3. Example of a localized automated continuum fit (top) and apparent column density profile (bottom) of the H I $\lambda 918$ transition observed at $z = 0.347925$ toward J000559.23+160948.9 (note that top and bottom x-axis scales are not the same). On the top panel, the red crosses mark points rejected during the continuum fit; the solid yellow line shows the Legendre polynomial fit to the continuum near the line of interest. The vertical dotted lines mark the integration range, while in the bottom panel, the red area marked the integrated column density profile. This type of figure was realized for each transition listed in Table 2 and was visually inspected to ensure that the continuum model was satisfactory.

with small-scale absorption or emission lines. Legendre polynomials of orders between 1 and 5 were fit to the remaining (non-rejected) pixels, with the goodness of the fit determining the adopted polynomial order. (Typically the adopted polynomials were of orders between 1 and 3 owing to the relative simplicity of the QSO continua when examined over velocity regions as small as $500\text{--}4000 \text{ km s}^{-1}$.) After a few tests, we realized that in several cases the continuum was not quite adequate near some absorption lines, in particular not rejecting completely the wings of the absorption lines. A second pass was necessary where the data were binned again and any binned pixels that were above or below 1.7σ below the original Legendre fit were rejected from the continuum placement regions. After several trials with different clipping values, we determined that the 1.7σ value allowed the algorithm to reject the highest number of non-continuum points, which includes unrelated absorbers and, most importantly, the tails of the absorption lines. This last part was crucial to getting a good fit to the continuum near the primary absorber itself. Figure 3 shows an example of the continuum fit around the H I $\lambda 918$ line observed at $z = 0.347925$ toward J000559.23+160948.9.

This procedure was applied to a predefined set of transitions (see Table 2), with the continuum defined locally for each. Each continuum model was visually inspected to ensure that it

was satisfactory. In a few cases, the automatic continuum fitting failed owing to a complex continuum (e.g., near the peak of an emission line or where many absorption lines were present within the predefined continuum window). In these cases, we first tried to adjust the velocity interval of the spectrum to provide better-constrained fits; if that still failed, we manually selected the continuum region to be fit.

4.2. Absorption Line Properties

The next step of the analysis was to integrate the absorption lines to determine the kinematic properties (central average velocities and linewidths), equivalent widths, and column densities for each absorption feature. The velocity range over which the line was integrated was determined from the H I absorption and, as much as possible, the integration corresponded to a single absorbing complex (at the COS resolution).

To estimate the column density, we use the AOD method. In this method, the absorption profiles are converted into AOD per unit of velocity, $\tau_a(v) = \ln[F_c(v)/F_{\text{obs}}(v)]$, where $F_c(v)$ and $F_{\text{obs}}(v)$ are the modeled continuum and observed fluxes as a function of velocity. The AOD, $\tau_a(v)$, is related to the apparent column density per unit of velocity, $N_a(v)$, through the relation $N_a(v) = 3.768 \times 10^{14} \tau_a(v) / (f\lambda(\text{\AA})) \text{ cm}^{-2} (\text{km s}^{-1})^{-1}$, where f is the oscillator strength of the transition and λ is the wavelength in \AA . The total column density is obtained by integrating the profile over the predefined velocity interval, $N = \int_{v_{\text{min}}}^{v_{\text{max}}} N_a(v) dv$, where $[v_{\text{min}}, v_{\text{max}}]$ are the boundaries of the absorption. We computed the average line centroids through the first moment of the AOD $v_a = \int v \tau_a(v) dv / \int \tau_a(v) dv \text{ km s}^{-1}$.

We characterize the total velocity widths of the absorption profiles by measuring the width Δv_{90} containing the central 90% of the integrated AOD in the line (i.e., Δv_{90} is the difference in velocity between the pixels at which 5% and 95% of the total optical depth has been reached; Prochaska & Wolfe 1997; Fox et al. 2013). For absorbers with several transitions of a given species detected at more than 2σ , we took a robust mean of the measurements, rejecting outliers more than 3σ from the median value (this is mainly useful for the H I transitions where weak and strong lines were compared).

We integrated the equivalent widths using the same $[v_{\text{min}}, v_{\text{max}}]$ integration range adopted for the $N_a(v)$ profiles. The main uses of the equivalent widths in our survey are twofold: (1) to determine if the absorption was detected at the $\geq 2\sigma$ level, and (2) to construct a curve-of-growth (COG) model for the H I absorption (see below). In cases where the line was detected at $\geq 2\sigma$ significance, the estimated apparent column density is adopted. Otherwise, we quote a 2σ upper limit on the column density, which is defined as twice the 1σ error derived for the column density assuming the absorption line lies on the linear part of the COG.

When an absorption feature is detected at $\geq 2\sigma$ significance, the AOD measurement may not represent the best estimate of the true column density, since it does not yet include an assessment of line contamination or saturation. We decided early in our survey that to embark into a complete line identification was not feasible owing to the large size sample and more importantly the incomplete wavelength coverage for many QSO spectra. Many spectra have gaps in the wavelength coverage and have only G130M or G160M observations. We assessed both line contamination and saturation using the procedures described in L13 and W16. Below we

describe the key steps and assumptions we made to determine the possible levels of contamination and saturation of an absorption feature.¹⁰

Our strategy for assessing whether a given transition is saturated or contaminated by another, unrelated absorber is based on a combination of visual inspection and comparison of the relevant quantities (e.g., mean velocity and apparent column density). Strong contamination can often be diagnosed visually, comparing the velocity structure of the absorption profiles across transitions from the same or similar ions (to determine if the main part of the absorption is at similar velocities or not). Our measurements of the mean velocities from the integration of the absorption profiles can often point to strong contamination (if the mean velocity from one transition is significantly different from others that are aligned). Typically, we allow for a 10–15 km s^{-1} uncertainty in the velocity in that comparison (owing to stretch in the COS wavelength solution). In the case of obvious contamination, the absorption feature is discarded. The only exception is if the contamination is very mild, only occurring in the wing of a relatively strong absorption; in that case, we slightly changed the velocity integration range to avoid the contaminated portion for that absorption feature. Similarly strong saturation where the apparent absorption reaches zero flux and the velocity profile can be reliably assessed visually (we made sure that there was no obvious sign of contamination in that case).

For less obvious contamination or saturation levels, the procedure depends on the number of transitions for a given ion or atom. For H I, both the saturation and contamination effects can be assessed reliably since several transitions are always available and several independent methods are used to determine the column density (AOD, COG, PF, and/or break at the Lyman limit, see Section 4.3). Similarly, some metal ions (e.g., O II, O III, and Si II) have several transitions with large enough λf -values to allow us to directly determine if there is some evidence for saturation or contamination. For atomic or ionic transitions that have $\Delta(\lambda f) \simeq 2$ and the difference in apparent column densities of the weak and strong transitions is $\Delta(\log N_a) \equiv \log N_a^{\text{weak}} - \log N_a^{\text{strong}} \leq 0.13$ dex (see W16), we were able to correct for the mild saturation using the method described in Savage & Sembach (1991) and W16. In this case, we report the apparent column densities for each transition and then the adopted column density, corrected for saturation. In cases where we were not able to correct for saturation, we report the column density as a lower limit determined by the AOD method and increased by 0.15 dex, which corresponds to the maximum saturation correction we can apply reliably (see W16).

To check for contamination in single transitions (in particular C III and Si III, which are critical for constraining

¹⁰ Our goal is to determine the metallicity of the weakly ionized gas that is observed over the same velocity interval as the strongest H I components. This requires that we accurately model the properties of at least the singly and doubly ionized species, if not those of the higher ions (such as, e.g., Si IV), depending on the H I column density of the absorber. Hence, although we have determined and report the column densities for higher ions (e.g., O IV and O VI), it is quite possible that our measurements do not represent an integration of the entire absorption profiles, since we only consider the absorption seen in the main H I absorption (i.e., the component that gives rise to at least one absorber with $\log N_{\text{H I}} \gtrsim 15.2$). One can refer to the figures in the Appendix to check the integration range for each reported ion. We caution the reader not to blindly use the column densities of the high ions reported in this work, which were derived for a very specific purpose, for issues beyond the metallicity of the main absorption complex. We will revisit the high-ion properties, and in particular O VI, in paper IV.

Table 3
Average Velocities and Column Densities of the Metal Ions
in the H I-selected Absorbers

Species	$[v_1, v_2]$ (km s ⁻¹)	$\langle v \rangle$ (km s ⁻¹)	$\log N$ ([cm ⁻²])
J000559.23+160948.9, $z = 0.305789$			
C II $\lambda 903$	-90, 70	...	<12.83
C III $\lambda 977$	-90, 70	34.5 \pm 8.8	12.93 \pm 0.07
Fe II $\lambda 2600$	-25, 25	...	<12.40
Fe III $\lambda 1122$	-90, 70	...	<13.43
H I $\lambda 926$	-90, 70	-5.7 \pm 8.2	15.35 \pm 0.09
H I $\lambda 937$	-90, 70	-7.3 \pm 3.1	15.30 \pm 0.03
H I $\lambda 949$	-90, 70	-7.0 \pm 1.5	15.35 \pm 0.02
H I AOD		-7.0 \pm 1.4	15.33 \pm 0.02
H I COG	15.34 \pm 0.03
H I FIT	15.33 \pm 0.02
H I AVG	15.33 \pm 0.01
Mg II $\lambda 2796$	-25, 25	...	<11.59
N I $\lambda 1199$	-90, 70	...	<13.09
N II $\lambda 1083$	-90, 70	...	<13.23
N V $\lambda 1238$	-90, 70	...	<13.20
O I $\lambda 1302$	-90, 70	...	<13.60
O VI $\lambda 1037$	-90, 70	...	<13.39
O VI $\lambda 1031$	-90, 70	-44.0 \pm 12.2	13.47 \pm 0.11
O VI		-44.0 \pm 12.2	13.47 \pm 0.11
S II $\lambda 1259$	-90, 70	...	<14.08
S III $\lambda 1012$	-90, 70	...	<13.57
S VI $\lambda 944$	-90, 70	...	<12.92
Si II $\lambda 1193$	-90, 70	...	<12.42
Si III $\lambda 1206$	-90, 70	...	<12.01

Note. Upper limits (<) are non-detections quoted at the 2σ level. Column densities preceded by > are lower limits owing to saturation in the absorption (lower limit values were increased by 0.15 dex to additionally correct for saturation, see the text for more detail). For a given atom or ion with more than one transition, we list in the row with no wavelength information the adopted weighted average column densities and velocities.

(This table is available in its entirety in machine-readable form.)

the ionization models), we first systematically checked for strong Milky Way contamination by comparing the observed wavelengths of the ions from the absorbers to the wavelengths of known Milky Way absorption lines (e.g., C II, Si II, Si III, N I, O I, and Fe II). Second, we used the information provided by atoms and ions with several transitions and the relative abundances. For the latter, while ionization obviously plays a role, one can deduce straightforwardly if absorption features are contaminated (e.g., if $N_{\text{N I}} \geq N_{\text{C II}}$ or $N_{\text{N II}} \geq N_{\text{C III}}$, then N I or N II are very likely contaminated, respectively). Using the information from these multiple transitions, we can also assess for a given absorber at what peak optical depth there is evidence for saturation; if there is for an ion or atom with only one available transition, the column density is reported as a lower limit with the 0.15 dex correction (see above).

The column densities, velocity integration ranges, averages velocities, and redshifts are summarized in Tables 3 and 4, which correspond to the new sample with $15.1 \lesssim \log N_{\text{H I}} < 19$ and the COS G130M and G160M absorbers from the L13 sample that were re-analyzed here (including any new ground-based spectra taken for this work), respectively. We also provide all the results in a machine-readable format (see the Appendix).

Table 4
Average Velocities and Column Densities of the Metal Ions
from the L13 Sample

Species	$[v_1, v_2]$ (km s ⁻¹)	$\langle v \rangle$ (km s ⁻¹)	$\log N$ ([cm ⁻²])
J015513.20-450611.9, $z = 0.225958$			
C II $\lambda 1036$	-100, 100	-2.6 \pm 2.9	14.08 \pm 0.03
C II $\lambda 1334$	-100, 100	14.4 \pm 3.9	14.05 \pm 0.04
C II		3.6 \pm 2.3	14.07 \pm 0.02
C III $\lambda 977$	-100, 100	2.9 \pm 0.9	>14.00
Fe II $\lambda 2600$	-50, 70	...	<12.25
H I $\lambda 930$	-100, 100	-8.9 \pm 3.2	>16.24
H I COG	16.79 \pm 0.08
H I LL	16.61 \pm 0.15
H I AVG	16.71 \pm 0.07
Mg II $\lambda 2796$	-50, 70	7.4 \pm 1.4	12.67 \pm 0.02
Mg II $\lambda 2803$	-50, 70	8.5 \pm 2.3	12.71 \pm 0.03
Mg II		7.7 \pm 1.2	12.68 \pm 0.02
N I $\lambda 1199$	-100, 100	...	<12.97
N II $\lambda 1083$	-100, 100	...	<13.11
N V $\lambda 1242$	-100, 100	...	<13.27
N V $\lambda 1238$	-100, 100	-31.6 \pm 14.6	13.31 \pm 0.11
N V		-31.6 \pm 14.6	13.31 \pm 0.11
O I $\lambda 976$	-100, 100	...	<14.71
O VI $\lambda 1031$	-100, 100	6.1 \pm 2.1	14.19 \pm 0.02
O VI $\lambda 1037$	-100, 100	7.8 \pm 4.8	14.16 \pm 0.04
O VI		6.3 \pm 1.9	14.18 \pm 0.02
S II $\lambda 1259$	-100, 100	...	<13.92
S III $\lambda 1012$	-100, 100	...	<13.57
S VI $\lambda 944$	-100, 100	...	<13.02
S III $\lambda 1190$	-100, 100	...	<13.79
Si II $\lambda 1190$	-100, 100	...	<12.71
Si II $\lambda 1260$	-100, 100	3.2 \pm 6.9	12.70 \pm 0.06
Si II		3.2 \pm 6.9	12.70 \pm 0.06
Si III $\lambda 1206$	-100, 100	6.5 \pm 0.9	>13.44
Si IV $\lambda 1393$	-100, 100	7.4 \pm 3.0	13.54 \pm 0.03
Si IV $\lambda 1402$	-100, 100	2.1 \pm 4.1	13.67 \pm 0.04
Si IV		5.6 \pm 2.4	13.57 \pm 0.02

Note. Upper limits (<) are non-detections quoted at the 2σ level. Column densities preceded by > are lower limits owing to saturation in the absorption (lower limit values were increased by 0.15 dex to additionally correct for saturation, see the text for more detail). For a given atom or ion with more than one transition, we list in the row with no wavelength information the adopted weighted average column densities and velocities.

(This table is available in its entirety in machine-readable form.)

4.3. H I Column Densities

To estimate the H I column density, we used several methods, which in part depended on the strength of the absorbers. For absorbers with $\log N_{\text{H I}} \gtrsim 16.8$ and where the H I column density is clearly dominated by a single component or where we cannot reliably estimate the column densities in the individual components of H I and metal ions, we used the flux decrement at the Lyman limit. For this method, we followed the procedure described in W16. In short, we estimated its redshift from the Lyman series lines. We then fitted the continuum on the red side of the break with a composite QSO spectrum (Telfer et al. 2002) and applied an artificial flux decrement at the wavelength of the break. We adjusted the modeled τ_{LL} to match the flux decrement (and recovery when possible) on the blue side of the break, producing an estimate for $N_{\text{H I}}$. The high-resolution data have high enough S/Ns that we could confidently fit the break at the

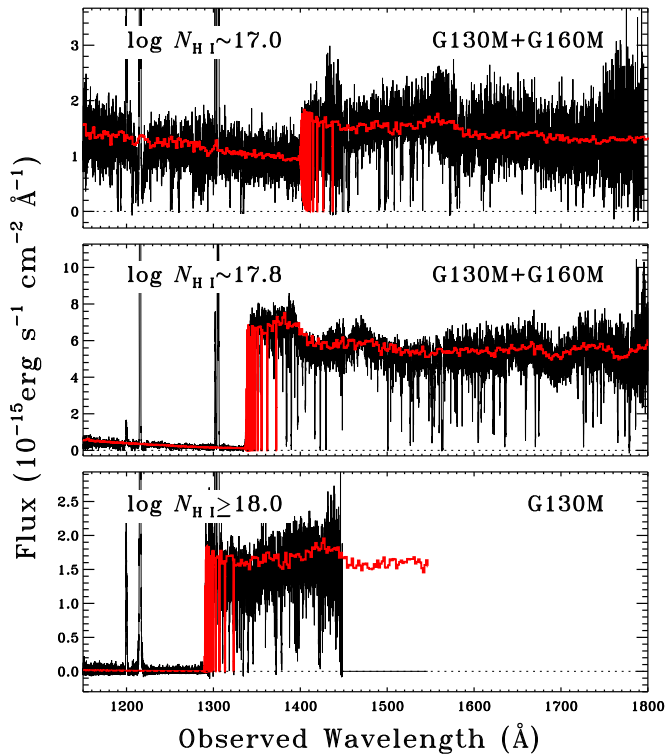


Figure 4. Examples of high-resolution spectra taken with COS G130M and G160M from our CCC survey. We show moderate- (top), high- (middle), and very high- $N_{\text{H I}}$ column density (saturated, in this case; bottom) absorption.

Lyman limit with little difficulty (given coverage of the continuum and recovery). The error on $N_{\text{H I}}$ is typically ~ 0.05 – 0.15 dex using this method for $\log N_{\text{H I}} \gtrsim 16.8$. In several cases, we also fitted the Lyman series lines with Voigt profiles (see below), and systematically found consistent results. The H I column densities derived using the break method have an LL line entry in Tables 3 and 4.

Depending on the complexity of the QSO continua and interstellar spectra (in particular near the Milky Way $\text{Ly}\alpha$ absorption), the method from the break at the Lyman limit can be used to determine $N_{\text{H I}}$ for absorbers with $\log N_{\text{H I}} \gtrsim 16.3$ or $\tau_{\text{LL}} \gtrsim 0.15$. However, for the typical S/N of the COS spectra (which is lower on average than the L13 sample), the break technique produces less accurate $N_{\text{H I}}$ than the other methods described below that use the Lyman series lines. We therefore only used this method as a verification step for absorbers with $16.3 \lesssim \log N_{\text{H I}} \lesssim 16.9$. In Figure 4, we show examples of this method for absorbers with different H I column densities. We overplot in red a composite QSO spectrum from Telfer et al. (2002) to which we have applied an artificial break at the adopted $N_{\text{H I}}$ as described above. The recovery at the blue end of each spectrum is useful for constraining $N_{\text{H I}}$ using the break, even when the continuum absorption and Lyman series lines are saturated near the break. However, at the highest column densities, the recovery is no longer present (see the bottom panel of Figure 4), and we could only derive a lower limit on $N_{\text{H I}}$. Therefore, we estimated the H I column densities of the absorbers using the decrement method only for absorbers with $16.9 \lesssim \log N_{\text{H I}} \lesssim 18$ (the exact value at the high end depends on how much flux recovery is available).

For absorbers with $15.2 \lesssim \log N_{\text{H I}} \lesssim 16.9$, we used a combination of different techniques to estimate $N_{\text{H I}}$, all using

the Lyman series transitions: the AOD method, PF, and COG. For the AOD method, we used all the available weak Lyman transitions that were not contaminated and for which the continuum could be reliably modeled. Typically for the weak Lyman transitions, the saturation effects are mild in the $15.2 \lesssim \log N_{\text{H I}} \lesssim 16.8$ range, but for the stronger absorbers or in cases where the weakest transitions are not available (owing to a lack of wavelength coverage or contamination), the COG and PF methods were favored to determine $N_{\text{H I}}$. In nearly all cases, we determined $N_{\text{H I}}$ with at least two transitions when we used the AOD; these transitions are summarized in Tables 3 and 4 (in the rare cases where we did not, the adopted $N_{\text{H I}}$ value is based only on the COG and PF methods). If there is no evidence of saturation, we averaged the values and propagated the errors accordingly, which is given in the H I AOD line entry in Tables 3 and 4. In the rare cases where there is evidence for saturation, we applied the method described in Section 4.2 to correct for it.

The COG method used a χ^2 minimization and χ^2 error derivation approach outlined by Sembach & Savage (1992). A single component COG is assumed. The program solves for $\log N$ and b independently in estimating the errors. We started with all the H I transitions for which we estimated the equivalent widths and did not appear a priori to be contaminated based on the AOD analysis. We checked the results from the COG model and then removed only the transitions clearly departing from the model. We ran our COG program again with the new set of transitions to obtain the final estimate of $N_{\text{H I}}$ with the COG method. Our adopted COG values are summarized in Table 3 in the COG line entry.

For the PF, we used a modified version of the software described in Fitzpatrick & Spitzer (1997), which is described in more detail in Lehner & Howk (2011) and Lehner et al. (2014). The same continua used in the COG and AOD methods were also used for the PF (i.e., the continuum placement was not a free parameter in the PF). A major difference from the previous methods is that the model profiles were convolved with the COS instrumental line-spread function. The three parameters for each component i (typically $i = 1$, but in some cases $i = 2$ or 3)—column density (N_i), Doppler parameter (b_i), and central velocity (v_i)—are input as initial guesses and were subsequently varied to minimize χ^2 of the fit to all the fitted H I transitions. In some rare cases the alignment of one or two transitions in a given absorber was somewhat off ($\gtrsim 20 \text{ km s}^{-1}$ relative to other transitions), and in these cases, the relative velocity of the departing transition was also allowed to vary during the fit. As for the COG, we started with all the H I transitions that did not appear a priori contaminated and iterated, removing any transitions that a posteriori appear contaminated or where a close absorption feature lies within the velocity range over which the χ^2 is estimated (we note that we could mask some of these features, but in all the cases we had enough H I transitions to accurately model $N_{\text{H I}}$ that we did not undertake this extra and more time-consuming step). In Figure 5, we show an example of PF that shows no contamination in many H I Lyman series transitions. Our adopted column densities from the PF are summarized in Table 3 in the FIT line entry.

In general, there was a good agreement between these different methods and we always use a combination of at least two of these methods, and in many cases the three methods, to estimate $N_{\text{H I}}$ for absorbers with $15.2 \lesssim \log N_{\text{H I}} \lesssim 16.9$. The

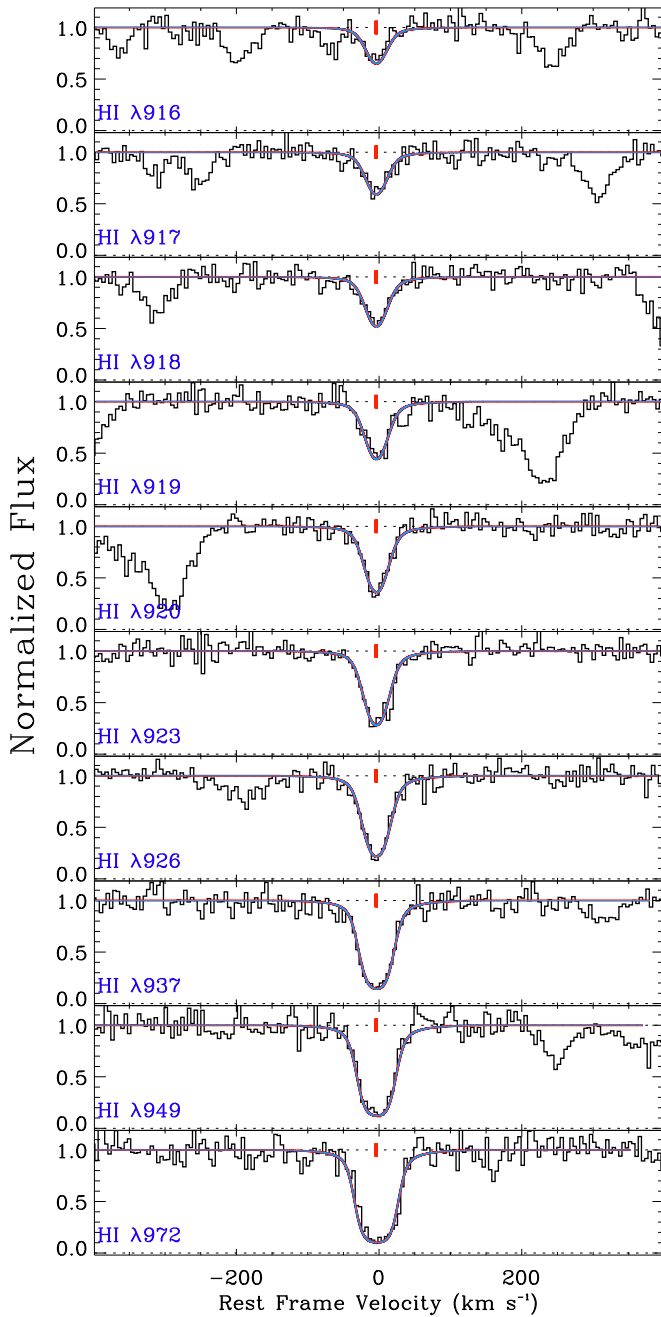


Figure 5. Example of a pLLS observed at $z = 0.347925$ toward J000559.23+160948.9 where we fitted the individual transitions of H I (black spectra) with a Voigt profile fit (red-blue solid lines). Note the large number of fitted H I transitions and the lack of any evidence for contamination in these transitions.

three methods explore different parameters and different transitions, allowing us to reliably estimate N_{HI} . We simply averaged the values and propagated the errors accordingly. Our adopted N_{HI} results are summarized in Table 3 in the AVG line entry.

Finally, for absorbers with $\log N_{\text{HI}} \gtrsim 18$, we generally could derive only a lower limit with the break method at the Lyman limit. In this case, we had to use further constraints to accurately determine N_{HI} , as the higher-order Lyman series lines remain saturated for many more transitions than the weaker H I absorbers. Only for absorbers where we have simultaneously Ly α and/or Ly β and very low H I transitions could we derive relatively accurate N_{HI} in that column density

Table 5
Sample of Absorbers Not Included in Our Sample

Name	z_{abs}	$\log N_{\text{HI}}$ (cm^{-2})
J100102.64+594414.2	0.303648	>18.00
J102117.47+343721.6	0.621005	>17.65
J102416.73+242211.6	0.522433	>18.10
J113327.78+032719.1	0.237384	>17.80
J123647.72+060048.4	0.540983	>18.05
J124035.51+094941.0	0.494686	>18.05
J124410.88+172104.6	0.550600	>17.85
J125224.99+291321.1	0.411039	>18.00
J131956.23+272808.2	0.660356	18.59 ± 0.05
J134251.60-005345.3	0.227331	>17.85
J161649.42+415416.3	0.320992	>17.90
J213135.20-120704.5	0.429789	>18.10

Note. All the absorbers with “>” in the H I column density column are lower limits, and hence absorbers for which we cannot reliably determine the metallicity. For J131956.23+272808.2, we derived a new H I column density based on the COS FUV and NUV data, but that absorber was originally Mg II selected and is therefore not included in our sample.

range (typical errors on N_{HI} are of order 0.2–0.3 dex for these strong H I absorbers). The Ly α absorption profile is particularly critical because at these amounts of H I the line profile begins to exhibit damping wings. The weaker transitions were used to make sure that the profile was not over-fit and the absence of some of the weakest H I transitions also helped in putting a lower limit on N_{HI} . Only five absorbers had the required transitions and S/N to accurately estimate N_{HI} at $\log N_{\text{HI}} \gtrsim 18$, and are summarized in Table 3. There were 11 additional absorbers where we could derive only a lower limit from the break and one that was originally Mg II selected (and hence is not in our final sample) that we list in Table 5 for completeness.

As noted in Section 3, there are two recent surveys that were undertaken with a smaller sample of COS data where N_{HI} was estimated (Stevens et al. 2014; Shull et al. 2017). The updated N_{HI} values in Shull et al. (2017) are in agreement with our own independent estimates within $1-2\sigma$, except for a few cases where the results from Stevens et al. (2014) are in better agreement (e.g., J124511.26+335610.1 at $z_{\text{abs}} = 0.556684$). We also note that some differences between these and our survey result from a different treatment of the velocity components whereby they sometimes combine more than one component in their estimate of the column densities (when we add the column densities of the various components in our survey, we would find essentially the same results).

Although it is always possible to have some errors in a large survey, we examined and analyzed the absorbers in a systematic way, and we used several methods to estimate N_{HI} , which explore different parameters and different transitions, adding confidence to our results. We also note that for the L13 sample that was revisited here, we found results that were consistent within less than $1-2\sigma$ despite using different sets of data (i.e., different data reduction and coaddition of the individual exposures) and an independent analysis.

5. Results

In this paper, we present results stemming directly from the estimated properties of the absorption for each absorber. In the subsequent papers, we will use photoionization models to

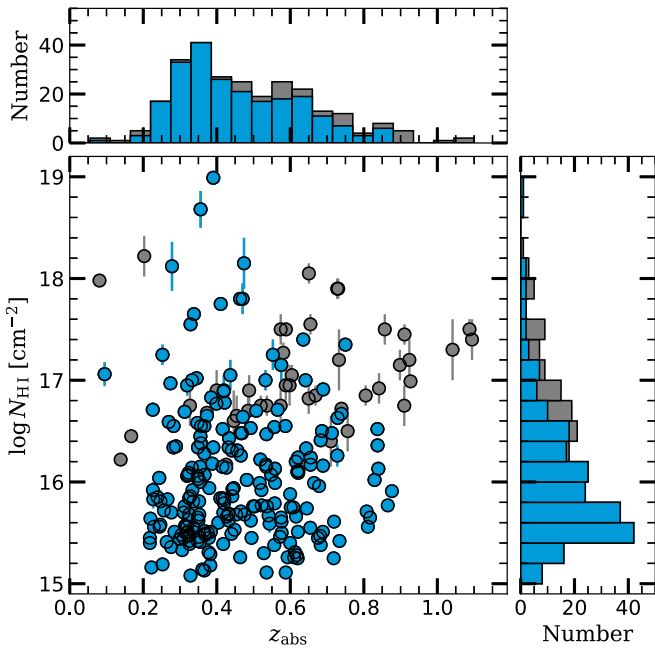


Figure 6. Scatter plot showing the distribution of the redshifts and H I column densities for the absorbers in our sample (blue data). The gray data show additional data from the samples analyzed in L13 and W16 that we did not revisit in this work. The top and right panels show the redshift and $\log N_{\text{HI}}$ distributions with the same color-coding definition.

interpret the data and, in particular, to estimate the metallicities of the absorbers. With just the column densities of metals and of H I, we show below that the gas with $15.1 \lesssim \log N_{\text{HI}} < 19$ is predominantly ionized; that there is evidence of multiphase gas; and that this gas has only very mild depletions of the heavy element Fe, to levels less than is observed in the Milky Way halo.

5.1. H I Column Density and Redshift Distributions of the Absorbers

In Figure 6, we show the distributions of the absorber redshifts and H I column densities. For the sample analyzed in this paper (shown in blue in this figure), the minimum ($z_{\text{min}} \sim 0.2$) and maximum ($z_{\text{max}} \sim 0.9$) redshifts are set by the observational constraints (COS wavelength bandpass and coverage of the H I Lyman series).¹¹ The redshifts largely overlap between the previous sample (i.e., the sample analyzed only in L13 and W16) and the newly analyzed sample here, except for a handful of absorbers at $0.9 \lesssim z_{\text{abs}} \lesssim 1.1$, which mostly come from the W16 sample. The mean redshift and standard deviation of the entire sample (blue and gray data points in Figure 6) are $\langle z_{\text{abs}} \rangle = 0.48 \pm 0.19$ (the median being $z_{\text{abs}} = 0.44$). Although the redshift distribution slightly peaks around $0.3 \lesssim z_{\text{abs}} < 0.4$, the overall redshift distribution is quite uniform in the range of $0.2 \lesssim z_{\text{abs}} \lesssim 0.7$. There is also no trend between z_{abs} and N_{HI} , i.e., a nearly 3 dex dispersion in N_{HI} is observed at any redshift in the interval of $0.2 \lesssim z_{\text{abs}} \lesssim 0.9$, although we note the lack of strong LLSs with $\log N_{\text{HI}} \gtrsim 18$ at $z_{\text{abs}} \gtrsim 0.5$ (see below).

¹¹ The only exception is the absorber at $z_{\text{abs}} = 0.09487$ observed toward J130532.99–103319.0 for which the N_{HI} estimate comes from *FUSE* observations (see Cooksey et al. 2008), but we analyzed here the metal transitions that are in the COS bandpass.

For N_{HI} , the entire sample ranges from $10^{15.08} - 10^{18.99} \text{ cm}^{-2}$. Absorbers with $\log N_{\text{HI}} \lesssim 16.2$ are only found in the new sample as our previous surveys did not target these absorbers. To the best of our knowledge, none of the absorbers with $15.1 \lesssim \log N_{\text{HI}} \lesssim 17$ were specifically targeted. These absorbers also do not produce a major break in the flux of the QSO spectra or produce major H I absorption features in low-resolution spectra and hence the background QSOs were potential targets to be observed with COS G130M and/or G160M. Therefore, the distribution of these absorbers should follow the overall distribution of the H I absorbers in column density, which can be described as a power law $f_{N_{\text{HI}}} \propto N_{\text{HI}}^{-\beta}$ at $z < 1$ (e.g., Lehner et al. 2007; Danforth et al. 2016); for a subset of the sample presented here, Shull et al. (2017) derived $\beta = 1.48 \pm 0.05$ for absorbers with $15 \lesssim \log N_{\text{HI}} \lesssim 17$. The number of absorbers at $\log N_{\text{HI}} \lesssim 15.3 - 15.4$ drops sharply; this is a pure artifact from our survey design since we are not complete below this threshold owing to the lack of sensitivity in the COS data to estimate low metallicities.

For absorbers with $17 \lesssim \log N_{\text{HI}} \lesssim 19$ and observed with COS G130M/G160M observations, the situation is more complicated since these absorbers can absorb part of or the entire UV flux, and many QSOs with known strong LLSs observed in low-resolution UV spectra might not have been targeted with the high-resolution mode of COS. However, our blind search of these LLSs identified more systems than we initially expected at least at $z_{\text{abs}} \lesssim 0.5$. We attribute this to the fact that many QSOs with no existing UV spectra prior to the COS observations were most certainly selected based on the FUV and NUV magnitudes obtained from the *Galaxy Evolution Explorer* (GALEX) mission. Since the GALEX FUV magnitude peaks around 1525 Å (and is most sensitive around 1420–1650 Å), a strong LLS can be present at $z \lesssim 0.5$ without any way of knowing this prior to the acquisition of a COS spectrum. Indeed, all the absorbers with $\log N_{\text{HI}} \geq 17.5$ (i.e., optically thick at the Lyman limit, $\tau_{\text{LL}} \geq 2$) in the new sample of strong LLSs have $z_{\text{abs}} < 0.5$ (although we note that four strong H I absorbers for which we could derive a lower limit on N_{HI} were found at $z > 0.5$, see Table 5; these may have been selected using a NUV or optical selection). Shull et al. (2017) found the same effect in their smaller sample where they did not find any LLSs with $\log N_{\text{HI}} \geq 17.2$ at $z_{\text{abs}} > 0.45$, attributing also this bias to the GALEX FUV pre-selection of the targets. We note, however, that the survey undertaken by W16 originally aimed to study the frequency of the LLSs at $0.4 \leq z_{\text{abs}} \leq 1$ selected the background QSOs based on their visual magnitude, and hence did not suffer from selection biases.

Therefore, our survey in the $15.4 \lesssim \log N_{\text{HI}} \leq 17.2$ range should follow the column density distribution of H I absorbers. In the range of $17.2 < \log N_{\text{HI}} < 19$, there is a bias against these absorbers at $0.5 \lesssim z_{\text{abs}} \lesssim 0.9$, but not at lower redshift. However, in this redshift interval, we also have several absorbers from our COS G140L survey (W16) (this survey covers only absorbers in the $0.4 \leq z_{\text{abs}} \leq 1$ range) where there is no bias against strong LLSs. Hence, the combined sample of absorbers with $15.4 \lesssim \log N_{\text{HI}} \lesssim 18$ should also follow closely the column density distribution at $z \lesssim 1$.

5.2. Velocity Widths and Doppler Parameters

We now consider the velocity widths of H I, low ions (C II and Mg II), and intermediate ions (C III). The velocity widths,

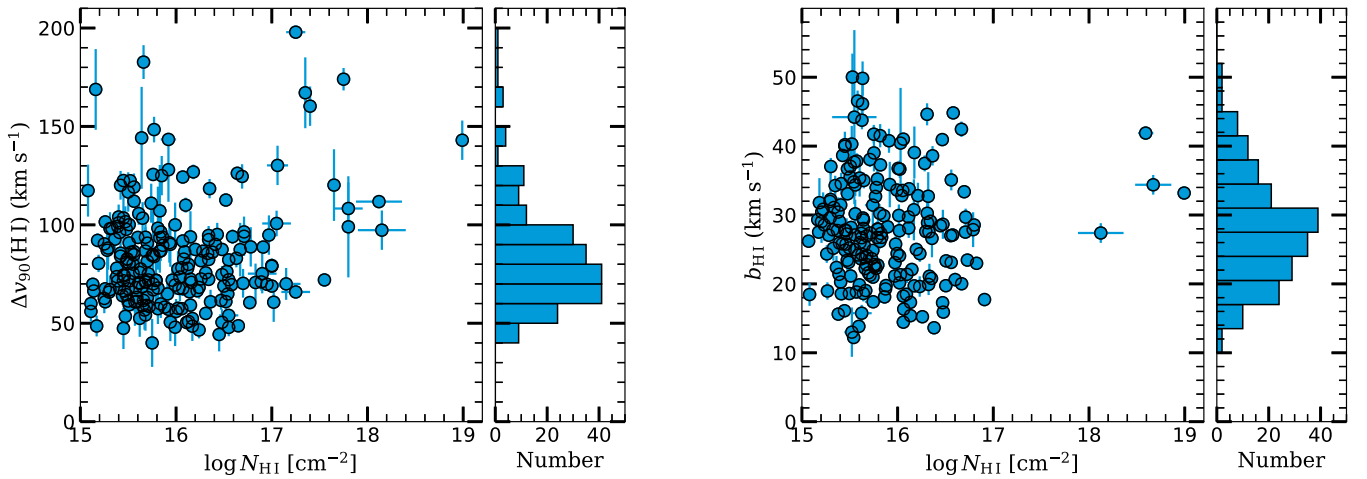


Figure 7. Left: comparison of the velocity width against the H I column density (Δv_{90} is obtained from the integration of the velocity profiles). Right: comparison of the Doppler parameters and $N_{\text{H I}}$ for the absorbers that were profile fitted.

Δv_{90} , were estimated using the same integration ranges that were used to determine the column densities. Although we provide information about the O VI (and other high ions), we remind the reader to treat these results with caution as we only integrated the profiles over the same velocity range. As shown by Fox et al. (2013) for the L13 sample of pLLSs and LLSs, the O VI profiles are typically broader than the low-ion profiles and their velocity centroids are offset from H I, indicating that O VI and H I do not necessarily coexist in the same regions (or have different weightings with velocity). This conclusion appears to be supported by the larger sample presented after inspecting the absorption velocity profiles in the Appendix, but further quantifying the differences between high and low ions is beyond the scope of our survey (but will be part of paper IV).

In the left panel of Figure 7, we compare the velocity width (Δv_{90}) of H I with $N_{\text{H I}}$. The velocity width ranges from 40–198 km s^{−1}, with 86% of the absorbers having $50 \leq \Delta v_{90} \leq 120$ km s^{−1} and the mean (and standard deviation) being 84 ± 27 km s^{−1}. The lower bound is unlikely to be an artifact since 40–50 km s^{−1} is 2–3 times the COS G130M and G160M resolution and since lower Δv_{90} are found in metal lines. For absorbers with $\log N_{\text{H I}} \lesssim 17$, there does not appear to be any trend between the velocity width and $N_{\text{H I}}$, and only 15% of the absorbers have $\Delta v_{90} > 100$ km s^{−1} in that $N_{\text{H I}}$ range. In contrast, 65% of the absorbers with $17 \lesssim \log N_{\text{H I}} \lesssim 19$ have $\Delta v_{90} > 100$ km s^{−1}. This reflects in part our inability to separate components at larger $N_{\text{H I}}$. However, there is no absorber in our sample with $\Delta v_{90} \gtrsim 200$ km s^{−1}, implying that these are extremely rare at $z \lesssim 1$ (but not at higher z , see Lehner et al. 2014; Lehner 2017 and Section 5.5).

In the right panel of Figure 7, we compare the Doppler parameter, b , and $N_{\text{H I}}$ derived from the PF in the individual components of H I. As for Δv_{90} , there is no trend between b and $N_{\text{H I}}$, which differs from the trend seen at $\log N_{\text{H I}} < 15$, where an increase of b with $N_{\text{H I}}$ is observed (although with a larger scatter, see Lehner et al. 2007). The mean and median values are 28 and 27 km s^{−1}, respectively, while the standard deviation is 7.8 km s^{−1}. The mean and median values are smaller than those seen in the Ly α forest (with $13.2 \leq \log N_{\text{H I}} \leq 14$) at similar redshifts where about 30% of the components consist of broad absorption ($b > 40$ km s^{−1}) (Lehner et al. 2007). In contrast, in our sample, 91% of the profile-fitted absorbers have $b < 40$ km s^{−1} and 16% have even

$b < 20$ km s^{−1}. We, however, note that the b -values for the eight absorbers with $\log N_{\text{H I}} \gtrsim 15$ in the Lehner et al. (2007) high-resolution survey ranges from about 15–50 km s^{−1}, fully consistent with our much larger survey.

The Doppler parameter for H I is related to the gas temperature via $b_{\text{H I}} = (2kT/m_{\text{H}} + b_{\text{nt}}^2)^{0.5}$, where k is the Boltzmann constant, T the temperature of the gas, m_{H} is the mass of hydrogen, and b_{nt} is the (unknown) nonthermal component to the broadening. Hence for $\langle b \rangle = 28$ km s^{−1}, the temperature of the gas is $T < 5 \times 10^4$ K and consistent with the gas being primarily photoionized.

In Figure 8, we show the velocity width of Mg II compared with the column densities of Mg II and H I. Seventy six percent of the absorbers have Δv_{90} values for Mg II in the 10–50 km s^{−1} range, a factor ~ 2 smaller than that of H I, but, as we argue below, this is mostly an instrumental resolution effect. Using the Spearman rank order, the test confirms the visual impression that there is a moderate positive monotonic correlation between $\Delta v_{90}(\text{Mg II})$ and the column densities of Mg II and H I (Spearman correlation coefficient $r_s = 0.43$ and 0.36 with a p -value $< 0.1\%$, respectively).¹² However, there is not a general increase of $\Delta v_{90}(\text{Mg II})$ with $N_{\text{Mg II}}$: large velocity profiles ($b > 50$ km s^{−1}) are only observed when $\log N_{\text{Mg II}} \gtrsim 12.5$, i.e., as $N_{\text{Mg II}}$ becomes larger, the number of Mg II components often increases. However, even as the column density of Mg II increases, a large fraction of the absorbers also has narrow and simple absorption profiles. The same trend is observed when comparing $\Delta v_{90}(\text{Mg II})$ and $N_{\text{H I}}$.

Finally in Figure 9, we compare the velocity widths of Mg II, C II, and C III with H I. There is a strong correlation between Δv_{90} of Mg II, C II, and C III with H I (Spearman correlation test $r_s \simeq 0.65$ with $p \ll 0.1\%$). For C II and C III with H I, the data are scattered around the 1:1 relationship. For Mg II, the data are scattered below the 1:1 relationship. In Table 6, we give the mean, standard deviation, and median of Δv_{90} for all these species and Si III. On average, Δv_{90} for Mg II is a factor ~ 2.2 smaller than that of C II, C III, or H I (Δv_{90} means, medians, and scatter are effectively the same for H I, C II, and C III), which is essentially the difference between the COS and high-resolution

¹² We adopt the following guide for the absolute value of r_s : 0.00–0.19: very weak, 0.20–0.39: weak, 0.40–0.59: moderate, 0.59–0.79: strong, and 0.80–1.00: very strong monotonic relationship.

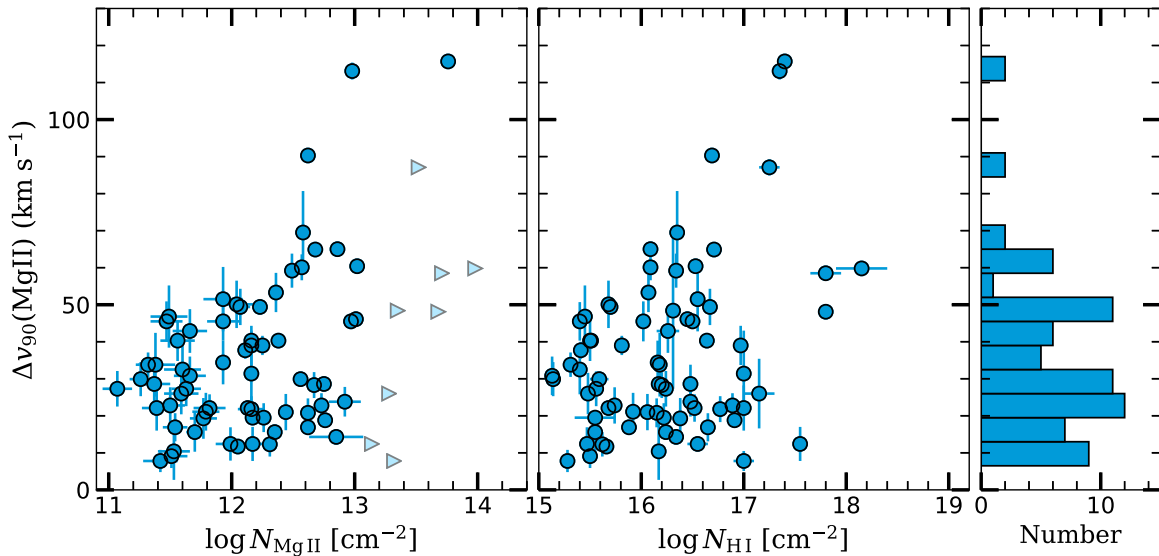


Figure 8. Comparison of the velocity width of Mg II with the Mg II and H I column densities.

ground-based observations. Hence, the difference observed between Mg II and the UV metal-line UV transition is an instrumental artifact, but it also implies that the typical values of Δv_{90} for the metal lines in the absorbers with $15 < \log N_{\text{H I}} < 19$ is close to $36 \pm 22 \text{ km s}^{-1}$.¹³

Although we do not show the comparison between the velocity centroids of H I and of C II, C III, and Mg II (and other low and intermediate ions), the dispersion in the centroid offsets between H I and low/intermediate ions is scattered around 0 km s^{-1} (see also Fox et al. 2013). All these arguments confirm the visual inspection of the absorption profiles that the H I and the low/intermediate trace the same gas and that the gas temperature is cool with $T \lesssim 5 \times 10^4 \text{ K}$.

5.3. Column Densities

With our results in hand, one of the most straightforward things to ask is how the metal ion column densities relate to those of H I. In Figure 10, we compare the column densities and equivalent widths of Mg II with the column densities of H I. The ranges of $N_{\text{Mg II}}$ and $W_{\text{Mg II}}$ are between <11 and >14 dex and <3 and 1100 mÅ , respectively. There is a visual strong correlation for both $N_{\text{Mg II}}$ and $W_{\text{Mg II}}$ with $N_{\text{H I}}$, which is confirmed by the Spearman correlation test $r_s \simeq 0.71$ and 0.57 , respectively, ($p \ll 0.1\%$; samples without upper limits—if the entire sample is considered instead, then $r_s \simeq 0.61$). The values at $\log N_{\text{Mg II}} \lesssim 12$ ($W_{\text{Mg II}} \lesssim 40 \text{ mÅ}$) are nearing our detection limit. For $\log N_{\text{Mg II}} \gtrsim 12$ ($W_{\text{Mg II}} \gtrsim 40 \text{ mÅ}$), there is a strong positive correlation between $N_{\text{Mg II}}$ and $W_{\text{Mg II}}$ with $N_{\text{H I}}$. There is a large range of $N_{\text{Mg II}}$ at all H I column densities. For example, over the range $16.0 \lesssim \log N_{\text{H I}} \lesssim 16.5$ there is a >2 dex spread in the observed values of $N_{\text{Mg II}}$.

In Figure 10, we also show as dashed lines in the top panel the general trends of metallicities from solar to -3 dex solar, which are adopted from the photoionization models shown in Figure 5 of W16. We have not updated these models and only use them here as guides to better understand the origin of the observed trends between Mg II and H I. As discussed in L13

and W16, the strength of Mg II depends strongly on $N_{\text{H I}}$ and the metallicity, but only weakly on the strength of the ionizing background. This is because the ionization correction for Mg II does not vary strongly over the range of ionization parameters probed by these absorbers owing to the similarity of the ionization potentials of H I and Mg II and a lack of strong spectral features in the UV radiation fields (W16; L13). As such, Mg II is a particularly good indicator of metallicity in the studied $N_{\text{H I}}$ range. The overall increase of $N_{\text{Mg II}}$ with increasing $N_{\text{H I}}$ is seen for absorbers with $-1 \lesssim [X/H] \lesssim 0$, i.e., metal-enriched systems. When $\log N_{\text{H I}} \gtrsim 17$, the Mg II $\lambda\lambda 2796, 2803$ doublet becomes more easily saturated, and the data cluster around the $[X/H] \simeq -1$ line (as we will see in paper II, with the addition of other ions we can more accurately and robustly estimate the metallicities for these absorbers). The scatter observed at $\log N_{\text{Mg II}} \lesssim 12$ is in part due to a sensitivity limit to low metallicity absorbers with Mg II, as there is a much larger fraction of upper limits when $15.2 \lesssim \log N_{\text{H I}} \lesssim 15.7$; in that range we can still detect metal-poor absorbers with $[X/H] \lesssim -1$, but not much below that (again this applies to Mg II alone; as we show in paper III, we can push below this limit using other metal ions). The lack of data around the $[X/H] \simeq -1$ line for absorbers with $16 \lesssim \log N_{\text{H I}} \lesssim 17$ is particularly interesting as it is around this value that the dip in the bimodal metallicity distribution of the pLLSs is observed (L13; W16; paper II). Interestingly, this feature is also clearly observed for the equivalent widths of Mg II where a hole in the scatter is seen for absorbers with $16 \lesssim \log N_{\text{H I}} \lesssim 17$. This demonstrates that the bimodal metallicity distribution in the $16 \lesssim \log N_{\text{H I}} \lesssim 17$ range is not an artifact of the ionization modeling. For $\log N_{\text{H I}} < 15.9$, we would need much better S/N ground-based spectra to improve the current limits on Mg II.

In Figure 11, we compare the column densities of C II, Si II, C III, and Si III with $N_{\text{H I}}$. Without the upper limits, the Spearman correlation test gives $r_s \simeq 0.83$ and 0.75 ($p \ll 0.1\%$) for C II and Si II, respectively, implying a very strong correlation between the column densities of the singly ionized species with $N_{\text{H I}}$ (these ranking numbers drop to 0.64 and 0.54 , respectively, if the upper limits are included). The sample with detections of C II is much smaller than that of Mg II and the upper limits are not as stringent, but there is also

¹³ We also note that Δv_{90} for H I, Si III, C II, and C III are essentially the same on average, implying that the atomic mass of species does not play a significant role in the broadening.

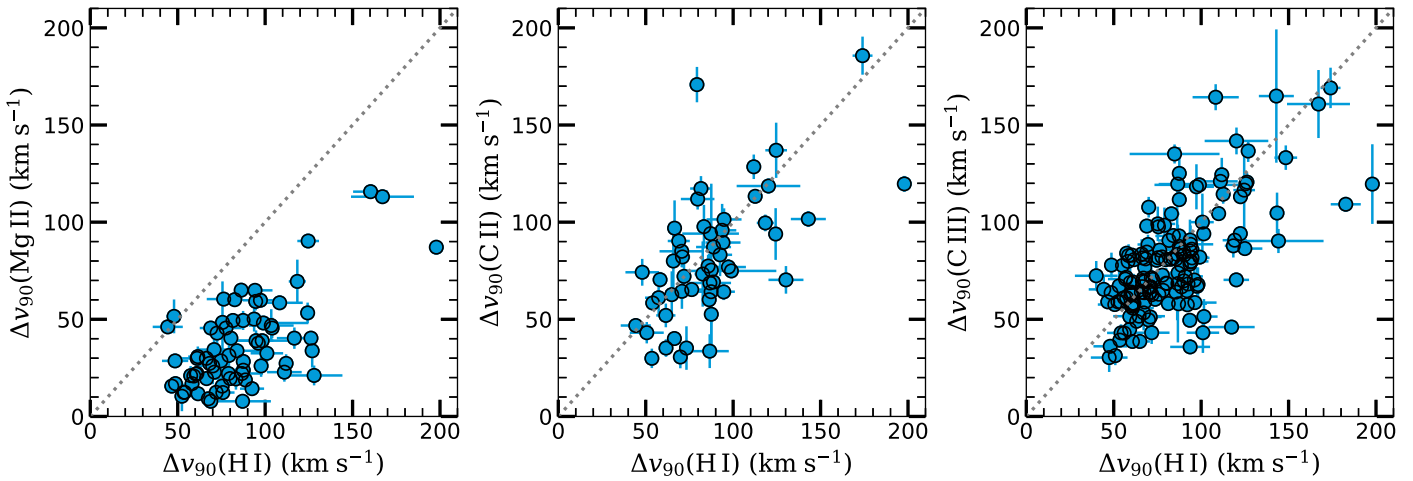


Figure 9. Comparison of the velocity widths of Mg II, C II, and C III with that of H I. The dotted line in each panel is the 1:1 relationship. Observations of Mg II have a resolution a factor ~ 2.2 better than the COS observations (C II, C III, and H I), explaining the observed difference.

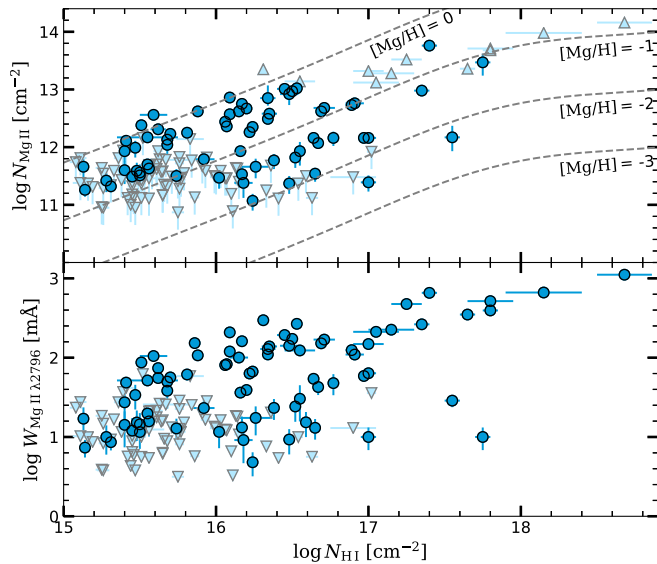


Figure 10. Column density of Mg II (top) and equivalent width of Mg II $\lambda 2796$ (bottom) compared with the column density of H I. The inverted triangles are 2σ upper limits, while the upright triangles are lower limits. In the top panel, the dashed lines represent the behavior of $N_{\text{Mg II}}$ with $N_{\text{H I}}$ in a photoionized gas with a solar (top) to 10^{-3} (bottom) solar metallicity.

Table 6

Summary of the Mean, Standard Deviation, and Median of Δv_{90}

Species	$\langle \Delta v_{90} \rangle$ (km s $^{-1}$)	$\Delta v_{90}^{1/2}$ (km s $^{-1}$)
H I	84 ± 27	78
C II	81 ± 32	76
C III	79 ± 27	78
Mg II	36 ± 22	30
Si III	88 ± 26	82

some evidence for a gap in the $N_{\text{C II}}$ distribution in the $16 \lesssim \log N_{\text{H I}} \lesssim 16.9$ range. For C III and Si III, the correlation is not as strong, but still significant with $r_s \simeq 0.5$ ($p \ll 0.1\%$). While there is a correlation between all these ions and H I, at any given $N_{\text{H I}}$ in the range of $15 \lesssim \log N_{\text{H I}} \lesssim 17$, there is a factor 10–30 (1–1.5 dex or more since some column densities

are lower limits) scatter in the column densities of the metal ions. At higher $N_{\text{H I}}$ ($\log N_{\text{H I}} \gtrsim 17.5$), except for one absorber, high metal column densities are observed. Both ionization and metallicity affect these column densities (and in particular C III and Si III are more dependent on the ionization parameter than the singly ionized species); however, as shown by L13 and W16 (and see papers II and III), the ionization parameter U does not change drastically in the H I column density range of $15 \lesssim \log N_{\text{H I}} \lesssim 19$. As implied by the analysis of W16 and confirmed with a larger sample in paper II, very low metallicity absorbers ($[X/H] \lesssim -1.4$) are rarer at $\log N_{\text{H I}} \gtrsim 17.5$, while common at lower $N_{\text{H I}}$, which explains in part the low and high scatter in the metal lines above and below $\log N_{\text{H I}} \simeq 17.5$, respectively.

Figures 10 and 11 also give a measure of the sensitivity of our survey for various key ions. For the singly ionized species, Mg II (with many upper limits at the level or lower than the detections) fairs typically better than C II and Si II (where many upper limits are quite high and overlap with relatively high columns of C II or Si II). The major difference is that the ground-based observations have a more uniform S/N than the COS observations. For C III, its $\lambda 977$ transition is so strong that the upper limits are scattered among the lowest column densities where C III absorption is detected. C III is also the ion with the lowest fraction of non-detections (11% of the sample) compared to 73%, 82%, 50%, and 30% for C II, Si II, Mg II, and Si III, respectively.

Typically, when C III is not detected, no other metals are detected. The exception is the absorber toward J135726.26 +043541.3 at $z = 0.328637$ ($\log N_{\text{H I}} = 17.55 \pm 0.05$), for which there are weak detections of the strong NUV transitions of Fe II and Mg II. As we will see in papers II and III, absorbers with no C III are among the lowest metallicity absorbers. Looking at Figure 11, there are only two absorbers with no C III (and no other metal ion detections) where the upper limits are well below the lowest detections. This implies that truly pristine gas at $z \lesssim 1$ is extremely rare with $<3\%$ (90% confidence level) of the absorbers with no metal detection. We will show in papers II and III that there is in fact no evidence for gas with $<1/1000$ solar metallicity at $z \lesssim 1$. At $z \sim 2\text{--}3.5$, pristine gas is rare too but not nonexistent with 3%–18% of the pLLSs/LLSs having no metals detected at levels $<1/10,000$ (Fumagalli et al. 2011a; Lehner et al. 2016). As shown in L13

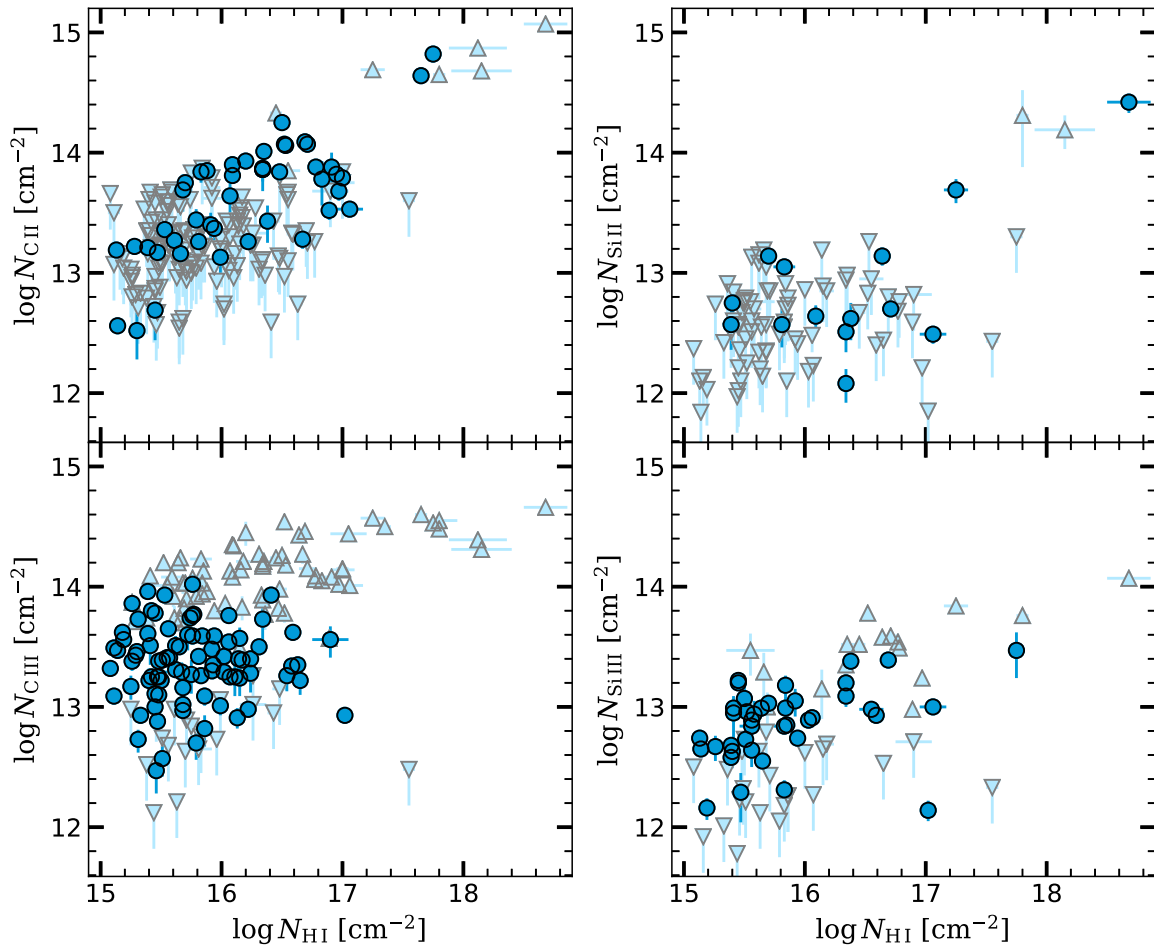


Figure 11. Column densities of selected key metal ions compared with the column density of H I. Inverted triangles are 2σ upper limits, while the upright triangles are lower limits.

and W16 and see also Figure 10, there is, however, a significant fraction of the absorbers that have metallicities $<1/100$ solar at $z \lesssim 1$, implying little enrichment for these absorbers over several billion years when compared to the metallicities of the same absorbers at $z \sim 2\text{--}3.5$ (see, Lehner et al. 2016).

5.4. Column Density Ratios

In Figure 12, we plot several ionic/atomic ratios as a function of N_{HI} . Depending on the species compared, these ratios inform us about the ionization or depletion levels of the gas. As we discuss below, some of these elements may also be affected by the nucleosynthetic history of the gas. We use the usual squared-bracket notation, $[X^{+i}/Y^{+j}] \equiv \log(N_{X^{+i}}/N_{Y^{+j}}) - [X/Y]_{\odot}$. Here X^{+i} and Y^{+j} represent elements X and Y in independent ionization stages i and j , while $[X/Y]_{\odot}$ represents the relative solar abundances of these elements (we use for the solar abundances from Asplund et al. 2009). No ionization corrections are applied in making these plots, so these values are sensitive both to relative ionization and abundance variations. Plotting these ratios as a function of N_{HI} allows us to determine if there is any trend with N_{HI} that could affect the metallicity comparison from low to high N_{HI} values.

For the H I column densities probed in our sample, $[\text{C II}/\text{Mg II}]$ is unlikely to be affected by dust depletion. In the Milky Way halo or the diffuse environment of the Magellanic Bridge, neither C nor Mg is strongly depleted

and their relative ratio should be roughly solar (e.g., Welty et al. 1999a; Lehner et al. 2001b; Lehner 2002; Lehner et al. 2008; Jenkins 2009). As discussed in L13 (and see also Lehner et al. 2016 for a similar behavior at high redshift), the $[\text{C}/\alpha]$ ratio is sensitive to nucleosynthesis effects with a time lag between the production of α elements (e.g., O, Si, and Mg) and carbon. However, as shown in L13 and further demonstrated with a larger sample in papers II and III, $[\text{C}/\alpha]$ is on average around the solar value with some scatter (about 0.35 dex). On average, results from Figure 12 show that $[\text{C II}/\text{Mg II}] = +0.37$. The super-solar value for $[\text{C II}/\text{Mg II}]$ is consistent with the gas being largely ionized since the ionization energies (IE) of C II are in the range 11.3–24.4 eV compared to Mg II 7.7–15.0 eV.

Similarly to C and Mg, O is very mildly depleted onto dust and the relative abundance of O relative to C or Mg should be about solar. Figure 12 shows that O I is not detected in the H I column density range $15 \lesssim \log N_{\text{HI}} \lesssim 19$, which is already a signature by itself that the gas must be largely ionized. Furthermore, for several absorbers, we were able to place strong upper limits on O I so that $[\text{O I}/\text{Mg II}]$ or $[\text{O I}/\text{C II}] \ll 0$, demonstrating that the gas is predominantly ionized without any ionization modeling (Lehner et al. 2001a, 2001b). For most of the absorbers, Figure 12 shows that $[\text{C III}/\text{C II}] \gtrsim 0$, also directly implying that the gas is ionized.

$[\text{C III}/\text{Si III}]$ is scattered around the solar value, which is consistent with the gas being photoionized by an ionizing source

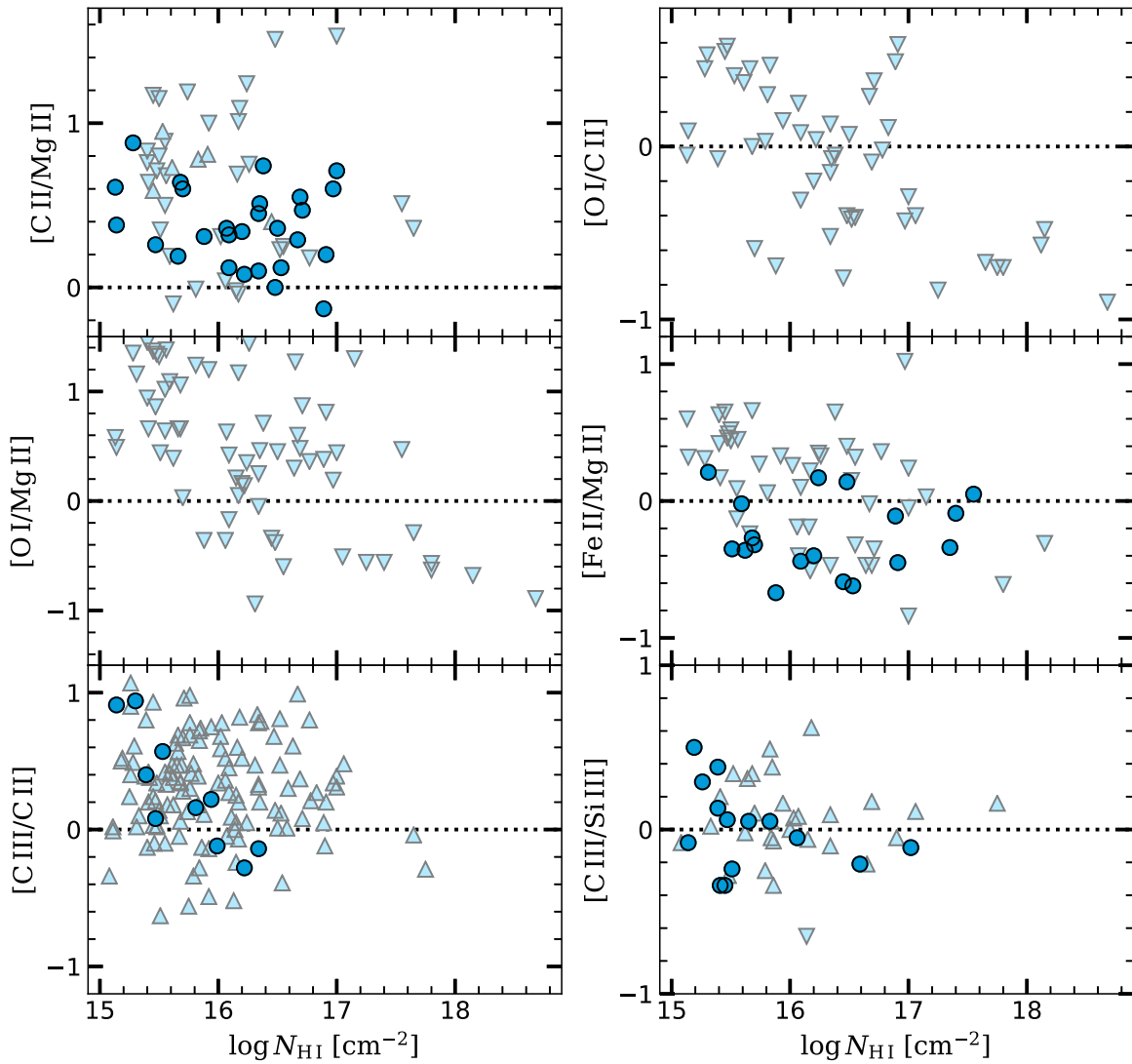


Figure 12. Ratios of various ions and atoms against the column density of H I (errorbars are not plotted but are, on average, about 0.10–0.15 dex on the y-scale). Inverted triangles are 2σ upper limits, while upright triangles are lower limits. The dotted line indicates the solar relative abundance in each panel. This set of panels implies that the gas is predominantly ionized and dust depletion is negligible for the absorbers in our sample.

that is not dominated by a hard ionizing spectrum (e.g., dominated by QSOs), otherwise we would expect $[\text{C III}/\text{Si III}] \gg 0$ (the IE range for C III is 24.4–47.9 eV compared to 16.3–33.5 eV for Si III). The scatter in the $[\text{C III}/\text{Si III}]$ ratio is consistent with the scatter we find in the $[\text{C}/\alpha]$ ratio (see papers II and III).

While ionization can affect the $[\text{Fe II}/\text{Mg II}]$ ratio, the effect should be small since they have similar ionization corrections over the densities probed by these absorbers and IE ranges (IE 7.9–16.2 for Fe II compared to Mg II 7.7–15.0 eV). The $[\text{Fe II}/\text{Mg II}]$ ratio can be, however, affected by dust depletion, where Fe is typically more depleted onto dust than Mg (e.g., Savage & Sembach 1996; Welty et al. 1999b; Jenkins 2009), or by nucleosynthesis, whereby an α -element can be enhanced relative to Fe in metal-poor environments such as in DLAs (e.g., Rafelski et al. 2012; Quiret et al. 2016). Only including the detections of Fe II, we find $\langle [\text{Fe II}/\text{Mg II}] \rangle = -0.25 \pm 0.27$. Using a survival analysis where the censored data (upper limits) are included (Feigelson & Nelson 1985; Isobe et al. 1986), we find $\langle [\text{Fe II}/\text{Mg II}] \rangle = -0.43 \pm 0.06$ (where the error is the error on the mean from the Kaplan–Meier estimator; the scatter being 0.30 dex). The scatter and mean are quite similar to the Fe/α seen in DLAs with

$[\alpha/\text{H}] \leq -1.5$ where $\langle [\text{Fe}/\alpha] \rangle = -0.5 \pm 0.3$ (see paper II). At the metallicities probed by these absorbers, both nucleosynthesis and depletion effects may play a role.

As mentioned above, iron is known to be depleted onto dust in the Milky Way, and it is the element that is the most affected by dust depletion in our sample (Savage & Sembach 1996; Welty et al. 1999b; Jenkins 2009).¹⁴ Jenkins (2009) found in the Milky Way for the lowest depletion factor ($F_* = 0$), the observed depletion of Mg and Fe are about -0.3 and -1 dex, respectively, corresponding to $[\text{Fe}/\text{Mg}] \simeq -0.7$.¹⁵ Figure 12 also shows no trend of $[\text{Fe II}/\text{Mg II}]$ with increasing N_{HI} , which would be expected if the depletion was important. The mean value $\langle [\text{Fe II}/\text{Mg II}] \rangle = -0.4 \pm 0.3$ implies the Fe depletion in the gas probed by the absorbers with $15 \lesssim \log N_{\text{HI}} \lesssim 19$ at

¹⁴ The comparison of the relative interstellar abundances of Fe relative to weakly depleted α elements in the Magellanic Cloud region (Welty et al. 1997, 1999a; Lehner et al. 2001b; Jenkins & Wallerstein 2017) and those in the Milky Way (Jenkins 2009) reveals comparable depletion patterns, despite global differences in the metal and dust content of these environments, which implies we can use the Milky Way results as a guideline.

¹⁵ As the depletion factor increases, $[\text{Fe}/\text{Mg}]$ decreases (e.g., if $F_* = 0.5$, then $[\text{Fe}/\text{Mg}] = -1$).

Table 7
Proximate Absorbers

Name	z_{em}	z_{abs}	Δv (km s^{-1})
J011935.69-282131.4	0.34886	0.348326	118.7
J011935.69-282131.4	0.34886	0.348731	28.7
J100110.20+291137.5	0.55800	0.556468	295.1
J110047.85+104613.2	0.42199	0.415099	1459.9
J122454.44+212246.3	0.43351	0.420788	2684.4
J122454.44+212246.3	0.43351	0.421357	2563.3
J124511.26+335610.1	0.71700	0.712976	704.3
J142735.59+263214.6	0.36600	0.366054	-11.9
J155048.29+400144.9	0.49684	0.491977	977.1
J155048.29+400144.9	0.49684	0.492632	845.2
J155232.54+570516.5	0.36600	0.366020	-4.4
J155232.54+570516.5	0.36600	0.366521	-114.3
J161916.54+334238.4	0.47093	0.470800	26.5

Note. Absorbers with $\Delta v \equiv (z_{\text{em}} - z_{\text{abs}})/(1 + z_{\text{abs}})c < 3000 \text{ km s}^{-1}$.

$z < 1$ are lower than the least-depleted environments in the Milky Way and Magellanic Clouds. Since α -enhancement can also affect this [Fe II/Mg II] ratio, the dust depletion effect could be even smaller. Therefore since Fe is the most refractory species studied in our sample, it also implies that dust depletion is negligible for all the absorbers in our sample.

Hence, there is some suggestion based on both [Fe II/Mg II] and [C III/Si III] (i.e., [C/ α]) that there is some nucleosynthetic enrichment history of the gas, in particular α -enhancement characteristic of nucleosynthesis from Type II supernovae. However, this effect is mild and not observed systematically in all the absorbers.

5.5. Proximate Absorbers and Multiple Component Absorbers

In our search for H I-selected absorbers, we did not reject a priori absorbers from our sample if their redshift was near the redshift of the QSO, i.e., $\Delta v \equiv (z_{\text{em}} - z_{\text{abs}})/(1 + z_{\text{abs}})c < 3000 \text{ km s}^{-1}$, where c is the speed of light. These are known as proximate absorbers (also known as “associated” absorbers although this is a misnomer since these absorbers may or may not be actually associated with the QSO). If several absorbers are closely separated in redshift space (that we defined as paired absorbers, keeping in mind that more than two absorbers can be closely separated in redshift space), we considered them separately as much as possible. We identify these paired absorbers because, depending on our finding for their metallicities, we will want to treat them as individual absorbers or combine them in our statistical sample. For example, if the metallicities of paired absorbers are always analogous, then it will show that there is not much metallicity variation along the line of sight in redshift space. On the other hand, if some paired absorbers have very different metallicities, it will indicate metallicity variation on a small redshift scale and we should not treat these paired absorbers as single absorbers.

In Tables 7 and 8, we list the proximate and paired absorbers, respectively. The immediate inference from these tables is that the effect (if any) of these absorbers on the global properties of the absorbers in our sample must be small since there are only 13 proximate absorbers and 30-paired absorbers in our total sample of 224 absorbers. Out of the 13 proximate absorbers, 8 are also paired absorbers, i.e., proximate absorbers with two

closely redshift-separated absorbers are more common (see Table 8). This is likely caused by the larger overdensity around QSOs, which can create an excess of H I absorption; such enhanced H I Ly α opacity has been observed toward $z \sim 2$ QSOs (e.g., Hennawi et al. 2006; Prochaska et al. 2013). Visually, the overall atomic and ionic velocity profiles of the proximate absorbers do not appear obviously different than the intervening absorbers ($\Delta v > 3000 \text{ km s}^{-1}$). The only exception is the absorber at $z = 0.470800$ toward J161916.54+334238.4 where there is extremely strong absorption of intermediate to high ions; in particular, the strong absorption features of S VI, S V, and S IV are not typically observed except in the proximity of a very hard ionizing source, implying that this particular absorber is likely an associated system.

Ten of the 30-paired absorbers have 3 (and one has 4) closely separated components. The individual H I column densities for these paired absorbers are below 10^{17} cm^{-2} , but this is an observational bias. Owing to the COS resolution, separating absorbers can be done more easily and robustly only for relatively low $N_{\text{H I}}$ absorbers. As shown in Figure 7 and discussed in Section 5.2, absorbers with $\log N_{\text{H I}} \gtrsim 17.2$ have typically larger Δv_{90} than absorbers with lower $N_{\text{H I}}$, corresponding to more complex velocity profiles with more than one component. In paper II where we determine the metallicity of the absorbers with $16.2 \leq \log N_{\text{H I}} < 19$, we will consider if there is any effect on the comparison of stronger and weaker $N_{\text{H I}}$ absorbers.

Finally, we note that our survey shows unambiguously how rare are SLFSs, pLLSs, or LLS with $\Delta v_{90} \geq 200\text{--}500 \text{ km s}^{-1}$ and a number of components $\gtrsim 5\text{--}10$ at $z < 1$. The only known reported cases are two LLSs at $z < 1$ (Tripp et al. 2011; Muzahid et al. 2015). This implies that only 1.5% (90% confidence level; 10% of the LLSs if only LLSs are considered) of the absorbers with $15 < \log N_{\text{H I}} < 19$ at $z \lesssim 1$ are very broad. This contrasts remarkably from the finding of the KODIAQ survey at high z where, with the same H I selection, more than 50% absorbers have $\Delta v_{90} \geq 200\text{--}500 \text{ km s}^{-1}$ and a number of components $\gtrsim 5\text{--}10$ at $z \sim 2\text{--}4$ (Lehner et al. 2014; Lehner 2017, and see also Simcoe et al. 2002, 2004). This suggests that a larger fraction of these high- z absorbers may probe large-scale outflows from high-redshift galaxies at an epoch where galaxies were forming stars at much higher rates.

6. Summary

Using the *HST* COS G130M and G160M archive, we have built the largest sample to date of H I-selected absorbers with $15 < \log N_{\text{H I}} < 19$ at $z \lesssim 1$ for which we can estimate the metallicities. The sample analyzed in this paper has 224 absorbers, and our total sample consists of 263 absorbers (where the additional data were observed *HST* STIS, *FUSE*, and *HST* COS). This survey is about an order of magnitude larger than the first survey of pLLSs and LLSs at $z < 1$ we undertook (L13), and it is the first survey targeting and analyzing absorbers with $15 < \log N_{\text{H I}} < 16.2$ in the same manner as the pLLSs and LLSs. More quantitatively, we increase the sample of pLLSs by a factor 2 (from 44 in W16 to 82) and of LLSs by a factor 2.6 (from 11 in W16 to 29), and assemble for the first time a sample of 152 SLFSs. The H I selection ensures that no bias is introduced in the metallicity distribution of these absorbers. We consider only absorbers with $\log N_{\text{H I}} > 15$ because the COS spectra of $z < 1$ QSO do

Table 8
Closely Redshift-separated Absorbers

Name	$[\log N_{\text{HI}}^1, \log N_{\text{HI}}^2]$ [cm ⁻²]	$[z_{\text{abs}}^1, z_{\text{abs}}^2]$	Δv_c (km s ⁻¹)	Type
J004705.89+031954.9	[15.57, 15.56]	[0.313870, 0.314257]	88.3	Int.
J011935.69-282131.4	[15.65, 16.03]	[0.348326, 0.348731]	90.1	Prox.
J020157.16-113233.1	[15.63, 15.47]	[0.322565, 0.323073]	115.2 ^a	Int.
J020157.16-113233.1	[15.47, 16.09]	[0.323073, 0.323404]	75.0 ^a	Int.
J020157.16-113233.1	[16.09, 15.84]	[0.323404, 0.324507]	249.9 ^a	Int.
J035128.56-142908.0	[16.38, 16.55]	[0.356924, 0.357173]	55.0	Int.
J044011.90-524818.0	[16.20, 15.66]	[0.614962, 0.615662]	129.9	Int.
J084349.47+411741.6	[17.00, 16.17]	[0.532565, 0.533507]	184.3	Int.
J094331.61+053131.4	[16.15, 16.00]	[0.354599, 0.354927]	72.6	Int.
J100102.64+594414.2	[15.84, 16.52]	[0.415649, 0.416042]	83.2	Int.
J100535.25+013445.5	[16.89, 15.79]	[0.418522, 0.419686]	246.0	Int.
J100535.25+013445.5	[16.52, 16.36]	[0.836989, 0.837390]	65.4 ^b	Int.
J100535.25+013445.5	[16.36, 16.13]	[0.837390, 0.839400]	328.0 ^b	Int.
J100902.06+071343.8	[16.45, 18.68]	[0.355352, 0.355967]	136.0	Int.
J102056.37+100332.7	[16.48, 16.26]	[0.464851, 0.465364]	105.0	Int.
J104117.16+061016.9	[15.55, 16.17]	[0.654403, 0.655059]	118.9 ^c	Int.
J104117.16+061016.9	[16.17, 16.24]	[0.655059, 0.655390]	60.0 ^c	Int.
J111754.23+263416.6	[15.81, 15.68]	[0.351969, 0.352307]	74.9	Int.
J112553.78+591021.6	[15.79, 16.13]	[0.557529, 0.558200]	129.2 ^d	Int.
J112553.78+591021.6	[16.13, 15.99]	[0.558200, 0.558450]	48.1 ^d	Int.
J113457.71+255527.8	[15.69, 16.34]	[0.431964, 0.432313]	73.1	Int.
J122454.44+212246.3	[15.83, 16.78]	[0.420788, 0.421357]	120.1	Prox.
J124511.26+335610.1	[16.16, 16.91]	[0.688948, 0.689370]	74.9	Int.
J134100.78+412314.0	[15.51, 16.09]	[0.620752, 0.621428]	125.0	Int.
J141038.39+230447.1	[15.62, 15.46]	[0.349849, 0.351043]	265.2	Int.
J150030.64+551708.8	[16.58, 15.42]	[0.347272, 0.347999]	161.8	Int.
J155048.29+400144.9	[16.53, 15.62]	[0.491977, 0.492632]	131.6	Prox.
J155232.54+570516.5	[16.28, 16.07]	[0.366020, 0.366521]	110.0	Prox.
J215647.46+224249.8	[15.25, 16.24]	[0.619964, 0.621016]	194.7	Int.
J215647.46+224249.8	[16.24, 16.11]	[0.621016, 0.621378]	66.9	Int.

Note. Absorbers with $\Delta v_c \equiv (z_{\text{abs}}^2 - z_{\text{abs}}^1)/(1 + z_{\text{abs}}^1)c < 500$ km s⁻¹ along the same sightline. ^a, ^b, ^c, ^d: sightlines with 3–4 closely redshift-separated absorbers. The last column indicates if the absorber is an intervening or proximate system.

not have high enough S/Ns to sensitively probe metallicity that is $\lesssim 10\%$ solar at lower column densities. For about half of our sample observed with COS G130M and/or G160M (113 absorbers), we have also high-resolution Keck HIRES and VLT UVES observations of the strong NUV transition of Mg II and Fe II NUV. All the measurements and spectra are made available online.

In subsequent papers, we will present the photoionization models used to determine the metallicity of these absorbers, the metallicity distributions of these absorbers, and the evolution of the metallicities over 7 orders of magnitude in N_{HI} ($15 < \log N_{\text{HI}} \lesssim 22$). We will also study how the properties of the high ions (in particular O VI) correlate with those of the low ions (paper IV). Here we have presented the basic measurements (column densities and kinematics) from the absorption of these absorbers to empirically characterize some of the properties of gas with $15 < \log N_{\text{HI}} < 19$ at $z \lesssim 1$. Our initial main findings are as follows:

1. From the comparison of the absorption profiles and the width of the profiles, we conclude low ions (singly and doubly ionized species) and H I trace the same gas. Thus, they can be modeled a priori with a single ionization phase model. This does not necessarily apply to the higher ions, and absorbers with high-ion absorption must

be multiphase. From the PF of the H I transitions, we show that on average the gas temperature is cool with $T < 5 \times 10^4$ K, which is consistent with the gas being photoionized.

2. The [Mg II/H I] ratio spans over 2 orders of magnitude at any N_{HI} over the range of $15 < \log N_{\text{HI}} < 19$, implying a metal enrichment from a solar to $\lesssim 1/100$ solar metallicity. We find that the absorbers are most likely all metal-enriched at some level, with only $< 3\%$ of the absorbers (90% confidence level) showing no metal absorption in the spectra. The bimodal metallicity distribution observed for the pLLSs in L13 and W16 is apparent from the Mg II column densities and equivalent widths, with a lack of data in the range $16.2 \lesssim \log N_{\text{HI}} \lesssim 17.2$ around a metallicity corresponding to about 10% solar. This corresponds to the previously observed dip in the metallicity distribution.
3. There is no strong dependence of the ionic ratios with N_{HI} . This implies that the ionization properties of the absorbers must not change dramatically over the range of $15 < \log N_{\text{HI}} < 19$ (4 orders of magnitude in N_{HI}).
4. We estimate $\langle [\text{Fe II}/\text{Mg II}] \rangle = -0.4 \pm 0.3$ comparable to that observed in DLAs at any z . This ratio can be affected by α -enhancement from Type II supernovae, which implies that Fe dust depletion is small if any. There is also no trend of the [Fe II/Mg II] ratio with N_{HI} , which might

be expected if dust depletion was a dominant factor. These findings demonstrate that depletion onto dust in these absorbers is negligible. On average we also show that $[C/\alpha]$ is consistent with a solar value, but with a large scatter of about 0.3 dex.

Support for this research was provided by NASA through grant *HST*-AR-12854 from the Space Telescope Science Institute, which is operated by the Association of Universities for Research in Astronomy, Incorporated, under NASA contract NAS5-26555. This material is also based upon work supported by the NASA Astrophysical Data Analysis Program (ADAP) grant NNX16AF52G. This work was supported by a NASA Keck PI Data Award, administered by the NASA Exoplanet Science Institute. Data presented herein were obtained at the W. M. Keck Observatory from telescope time allocated to NASA through the agency’s scientific partnership with the California Institute of Technology and the University of California. The Observatory was made possible by the generous financial support of the W. M. Keck Foundation. K.L.C. acknowledges support from NSF Grant No. AST-1615296 and appreciates the observational support of K. Cannoles and T. Wells, University of Hawaii at Hilo undergraduate students. Some of the data presented in this work were obtained from KODIAQ, which was funded through NASA ADAP Grant Nos. NNX10AE84G and NNX16AF52G. This research has made use of the KOA, which is operated by the W. M. Keck Observatory and the NASA Exoplanet Science Institute (NExScI), under contract with NASA. The authors wish to recognize and acknowledge the very significant cultural role and reverence that the summit of Maunakea has always had within the indigenous Hawaiian community. We wish to acknowledge and thank all the NASA personnel, and in particular the astronauts, who made the servicing mission 4 on the *HST* a complete success. Their dedication has revolutionized our understanding of the importance of the CGM in the formation and evolution of galaxies and many other fields.

Facilities: *HST* (COS), Keck (HIRES), LBT (MODS), VLT:Kueyen (UVES).

Appendix

In this Appendix, we provide some information regarding the supplemental items. First, for each absorber studied in this paper, we produced a figure as shown in Figure 13 where we plot the normalized profiles of metals and weak H I transitions for which we estimated the column densities. The red portion in each profile shows the velocity range of the absorption over which the velocity profile was integrated to derive the column densities and kinematics (average velocity and linewidth). The vertical dashed lines mark the zero velocity.

Second we provide the results in a machine-readable format in Table 9. The first two columns provide the J name and the *HST* name. Columns 3 and 4 give the redshift and its error; Column 5 gives the ion; Columns 6 and 7 the minimum and maximum velocities for the integration range, Columns 8 and 9 the average velocity and its error, Columns 10, 11, and 12 the column densities and upper and lower errors. The last three columns in Table 9 correspond to detection, upper and lower limits (flag = 0, −1, −2, respectively), reliability of the detection depending if a single or several transitions were detected ((1) results based on several transitions or a non-detection, which is always reliable since it would be estimated in an uncontaminated region of the spectrum; (2) results based on at least two transitions, but where only one transition is detected at the 2σ level and the upper limits agree with that detection; (3) results based only on a single transition or several saturated transitions), and a unique identification number of the absorber. In that table, a “999.0” value in the average velocity and error columns corresponds to no absorption observed at the 2σ level, and hence that entry is an upper limit on the column density.

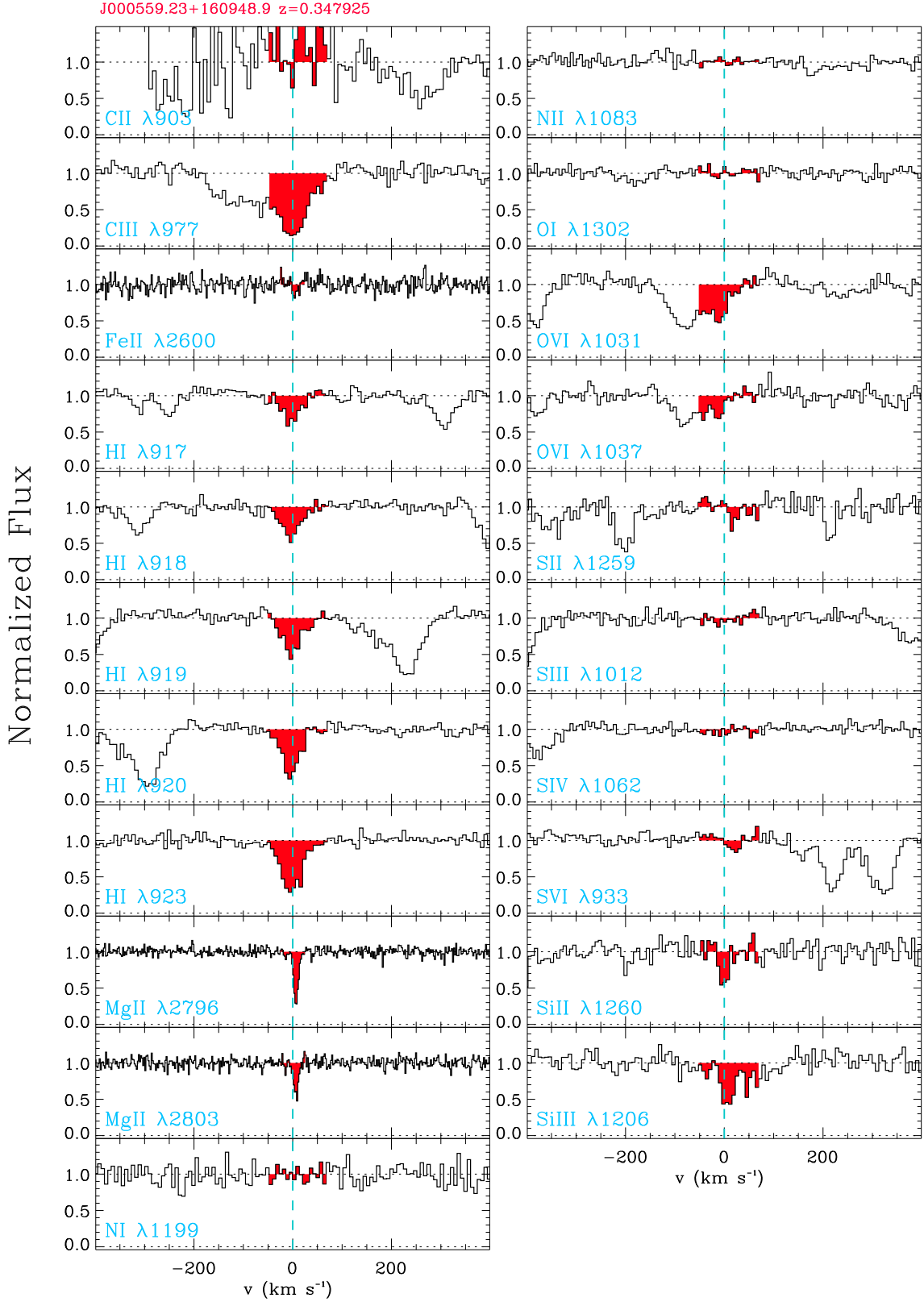


Figure 13. Normalized absorption lines as a function of rest-frame velocity centered on the absorber at $z = 0.347925$ toward J000559.23+160948.9. The EUV and UV transitions are from COS G130M and G160M and Mg II and Fe II NUV transitions are in this case Keck HIRES spectra. The red portion in each profile shows the velocity range of the absorption over which the velocity profile was integrated to derive the column densities, equivalent widths, and kinematics. The vertical dashed lines mark the zero velocity. Note in this case the simplicity of the velocity profiles in most of the ions and weak H I transitions; only in C III and O VI is there evidence of another absorber at ~ -100 km s $^{-1}$ (that absorption is only observed in the strongest H I transitions—Ly α and Ly β , implying $\log N_{\text{H I}} \lesssim 14$ for that absorber). (The complete figure set (224 images) is available.)

Table 9
Summary of the Results in Machine-readable Format

Name	<i>HST</i> Name	z_{abs}	$\sigma_{z_{\text{abs}}}$	Ion	v_1 (km s ⁻¹)	v_2 (km s ⁻¹)	$\langle v \rangle$ (km s ⁻¹)	$\sigma_{\langle v \rangle}$ (km s ⁻¹)	$\log N$ ([cm ⁻²])	$\sigma_{\log N}^{\text{upper}}$ ([cm ⁻²])	$\sigma_{\log N}^{\text{lower}}$ ([cm ⁻²])	Detection Flag	Reliability Flag	Unique ID
(1)	(2)	(3)	(4)	(5)	(6)	(7)	(8)	(9)	(10)	(11)	(12)	(13)	(14)	(15)
J000559.23+160948.9	PG0003+158	0.305789	0.000029	Al II	-90.0	70.0	999.0	999.0	15.00	0.18	0.30	-1	3	1
J000559.23+160948.9	PG0003+158	0.305789	0.000029	Ar I	-90.0	70.0	999.0	999.0	12.83	0.18	0.30	-1	3	1
J000559.23+160948.9	PG0003+158	0.305789	0.000029	C II	-90.0	70.0	999.0	999.0	12.83	0.18	0.30	-1	3	1
J000559.23+160948.9	PG0003+158	0.305789	0.000041	C III	-90.0	70.0	34.5	8.8	12.93	0.06	0.07	0	1	1
J000559.23+160948.9	PG0003+158	0.305789	0.000029	*C II	-90.0	70.0	999.0	999.0	13.04	0.18	0.30	-1	3	1
J000559.23+160948.9	PG0003+158	0.305789	0.000029	Fe II	-25.0	25.0	999.0	999.0	12.40	0.18	0.30	-1	3	1
J000559.23+160948.9	PG0003+158	0.305789	0.000029	Fe III	-90.0	70.0	999.0	999.0	13.43	0.18	0.30	-1	3	1
J000559.23+160948.9	PG0003+158	0.305789	0.000040	H I	-90.0	70.0	-7.1	1.4	15.33	0.02	0.01	0	3	1
J000559.23+160948.9	PG0003+158	0.305789	0.000029	Mg II	-25.0	25.0	999.0	999.0	11.59	0.18	0.30	-1	3	1
J000559.23+160948.9	PG0003+158	0.305789	0.000029	N I	-90.0	70.0	999.0	999.0	13.09	0.18	0.30	-1	3	1
J000559.23+160948.9	PG0003+158	0.305789	0.000029	N II	-90.0	70.0	999.0	999.0	13.23	0.18	0.30	-1	3	1
J000559.23+160948.9	PG0003+158	0.305789	0.000029	N V	-90.0	70.0	999.0	999.0	13.20	0.18	0.30	-1	3	1
J000559.23+160948.9	PG0003+158	0.305789	0.000029	O I	-90.0	70.0	999.0	999.0	13.60	0.18	0.30	-1	3	1
J000559.23+160948.9	PG0003+158	0.305789	0.000050	O VI	-90.0	70.0	-44.0	12.2	13.47	0.09	0.11	0	2	1
J000559.23+160948.9	PG0003+158	0.305789	0.000029	S II	-90.0	70.0	999.0	999.0	14.08	0.18	0.30	-1	3	1
J000559.23+160948.9	PG0003+158	0.305789	0.000029	S III	-90.0	70.0	999.0	999.0	13.57	0.18	0.30	-1	3	1
J000559.23+160948.9	PG0003+158	0.305789	0.000029	S VI	-90.0	70.0	999.0	999.0	12.92	0.18	0.30	-1	3	1
J000559.23+160948.9	PG0003+158	0.305789	0.000029	Si II	-90.0	70.0	999.0	999.0	12.42	0.18	0.30	-1	3	1
J000559.23+160948.9	PG0003+158	0.305789	0.000029	Si III	-90.0	70.0	999.0	999.0	12.01	0.18	0.30	-1	3	1
J000559.23+160948.9	PG0003+158	0.347925	0.000029	Ar I	-50.0	70.0	999.0	999.0	12.65	0.18	0.30	-1	3	2
J000559.23+160948.9	PG0003+158	0.347925	0.000034	C II	-50.0	70.0	999.0	999.0	13.40	0.18	0.30	-1	3	2
J000559.23+160948.9	PG0003+158	0.347925	0.000029	C III	-50.0	70.0	0.2	0.9	13.76	0.01	0.02	0	1	2
J000559.23+160948.9	PG0003+158	0.347925	0.000029	Fe II	-25.0	25.0	999.0	999.0	12.17	0.18	0.30	-1	3	2
J000559.23+160948.9	PG0003+158	0.347925	0.000029	Fe III	-50.0	70.0	999.0	999.0	13.32	0.18	0.30	-1	3	2
J000559.23+160948.9	PG0003+158	0.347925	0.000033	H I	-50.0	70.0	-2.4	1.0	16.06	0.01	0.01	0	3	2
J000559.23+160948.9	PG0003+158	0.347925	0.000029	Mg II	-25.0	25.0	6.0	0.9	12.44	0.03	0.03	0	3	2
J000559.23+160948.9	PG0003+158	0.347925	0.000029	N I	-50.0	70.0	999.0	999.0	13.20	0.18	0.30	-1	3	2
J000559.23+160948.9	PG0003+158	0.347925	0.000029	N II	-50.0	70.0	999.0	999.0	13.04	0.18	0.30	-1	3	2
J000559.23+160948.9	PG0003+158	0.347925	0.000029	O I	-50.0	70.0	999.0	999.0	13.24	0.18	0.30	-1	3	2
J000559.23+160948.9	PG0003+158	0.347925	0.000030	O VI	-50.0	70.0	-19.0	2.5	13.97	0.03	0.03	0	3	2
J000559.23+160948.9	PG0003+158	0.347925	0.000029	S II	-50.0	70.0	999.0	999.0	14.04	0.18	0.30	-1	3	2
J000559.23+160948.9	PG0003+158	0.347925	0.000029	S III	-50.0	70.0	999.0	999.0	13.53	0.18	0.30	-1	3	2
J000559.23+160948.9	PG0003+158	0.347925	0.000047	S IV	-50.0	70.0	3.1	11.2	13.45	0.13	0.18	-1	3	2
J000559.23+160948.9	PG0003+158	0.347925	0.000029	S VI	-50.0	70.0	999.0	999.0	12.54	0.18	0.30	-1	3	2
J000559.23+160948.9	PG0003+158	0.347925	0.000041	Si II	-50.0	70.0	3.4	8.9	12.48	0.10	0.14	-1	3	2
J000559.23+160948.9	PG0003+158	0.347925	0.000031	Si III	-50.0	70.0	15.7	3.2	12.91	0.04	0.05	0	1	2
J000559.23+160948.9	PG0003+158	0.366204	0.000029	Al II	-50.0	50.0	999.0	999.0	14.75	0.18	0.30	-1	3	3
J000559.23+160948.9	PG0003+158	0.366204	0.000029	Ar II	-50.0	50.0	999.0	999.0	13.87	0.18	0.30	-1	3	3
J000559.23+160948.9	PG0003+158	0.366204	0.000032	C II	-50.0	50.0	-9.8	3.4	13.19	0.05	0.06	0	3	3
J000559.23+160948.9	PG0003+158	0.366204	0.000029	Fe II	-25.0	25.0	999.0	999.0	12.18	0.18	0.30	-1	3	3
J000559.23+160948.9	PG0003+158	0.366204	0.000029	Fe III	-50.0	50.0	999.0	999.0	13.32	0.18	0.30	-1	3	3
J000559.23+160948.9	PG0003+158	0.366204	0.000037	H I	-50.0	50.0	1.6	0.6	15.13	0.01	0.01	0	3	3
J000559.23+160948.9	PG0003+158	0.366204	0.000033	Mg II	-25.0	25.0	3.2	5.2	11.66	0.13	0.19	0	2	3
J000559.23+160948.9	PG0003+158	0.366204	0.000029	N I	-50.0	50.0	999.0	999.0	13.28	0.18	0.30	-1	3	3
J000559.23+160948.9	PG0003+158	0.366204	0.000029	N II	-50.0	50.0	999.0	999.0	13.02	0.18	0.30	-1	3	3
J000559.23+160948.9	PG0003+158	0.366204	0.000031	N III	-50.0	50.0	-2.2	3.3	13.66	0.05	0.06	0	1	3

Table 9
(Continued)

Name	<i>HST</i> Name	z_{abs}	$\sigma_{z_{\text{abs}}}$	Ion	v_1 (km s ⁻¹)	v_2 (km s ⁻¹)	$\langle v \rangle$ (km s ⁻¹)	$\sigma_{(v)}$ (km s ⁻¹)	$\log N$ ([cm ⁻²])	$\sigma_{\log N}^{\text{upper}}$ ([cm ⁻²])	$\sigma_{\log N}^{\text{lower}}$ ([cm ⁻²])	Detection Flag (13)	Reliability Flag (14)	Unique ID (15)
(1)	(2)	(3)	(4)	(5)	(6)	(7)	(8)	(9)	(10)	(11)	(12)	(13)	(14)	(15)
J000559.23+160948.9	PG0003+158	0.366204	0.000037	N V	-50.0	50.0	-17.9	7.1	13.43	0.09	0.11	0	2	3
J000559.23+160948.9	PG0003+158	0.366204	0.000029	O I	-50.0	50.0	999.0	999.0	13.40	0.18	0.30	-1	3	3
J000559.23+160948.9	PG0003+158	0.366204	0.000029	O II	-50.0	50.0	999.0	999.0	13.53	0.18	0.30	-1	3	3
J000559.23+160948.9	PG0003+158	0.366204	0.000030	O III	-50.0	50.0	3.9	2.7	14.55	0.04	0.05	0	1	3
J000559.23+160948.9	PG0003+158	0.366204	0.000029	O VI	-50.0	50.0	-3.1	1.1	14.01	0.02	0.02	0	3	3
J000559.23+160948.9	PG0003+158	0.366204	0.000029	S II	-50.0	50.0	999.0	999.0	13.93	0.18	0.30	-1	3	3
J000559.23+160948.9	PG0003+158	0.366204	0.000029	S III	-50.0	50.0	999.0	999.0	13.48	0.18	0.30	-1	3	3
J000559.23+160948.9	PG0003+158	0.366204	0.000038	S VI	-50.0	50.0	999.0	999.0	12.55	0.18	0.30	-1	3	3
J000559.23+160948.9	PG0003+158	0.366204	0.000029	Si II	-50.0	50.0	999.0	999.0	12.10	0.18	0.30	-1	3	3
J000559.23+160948.9	PG0003+158	0.366204	0.000030	Si III	-50.0	50.0	5.8	2.7	12.74	0.05	0.05	0	1	3

Note. A 999.0 value corresponds to a non-detection 2σ level and the upper limit on the column density is quoted at the 2σ level. The detection flag has the following definition: 0 = detection; -1 = upper limit (non-detection); -2 = detection but a lower limit owing to saturation of the line. Depending if a single or several transitions were detected, a reliability flag is assigned as follows: 1 = most reliable: results based on several transitions or a non-detection (a non-detection always reliable since it is estimated in an uncontaminated region of the spectrum); 2 = reliable: results based on at least two transitions, but where only one transition is detected at the 2σ level and the upper limits agree with that detection; 3 = less reliable: results based only on a single transition or several saturated transitions.

(This table is available in its entirety in machine-readable form.)


ORCID iDs

Nicolas Lehner  <https://orcid.org/0000-0001-9158-0829>

Christopher B. Wotta  <https://orcid.org/0000-0001-6923-978X>

J. Christopher Howk  <https://orcid.org/0000-0002-2591-3792>

John M. O'Meara  <https://orcid.org/0000-0002-7893-1054>

Benjamin D. Oppenheimer  <https://orcid.org/0000-0002-3391-2116>

References

- Asplund, M., Grevesse, N., Sauval, A. J., & Scott, P. 2009, *ARA&A*, **47**, 481
- Berg, D. A., Skillman, E. D., Henry, R. B. C., Erb, D. K., & Carigi, L. 2016, *ApJ*, **827**, 126
- Bielby, R., Crighton, N. H. M., Fumagalli, M., et al. 2017, *MNRAS*, **468**, 1373
- Bowen, D. V., Pettini, M., & Blades, J. C. 2002, *ApJ*, **580**, 169
- Cantalupo, S. 2017, *ASSL*, **430**, 195
- Chen, H.-W., Prochaska, J. X., Weiner, B. J., Mulchaey, J. S., & Williger, G. M. 2005, *ApJL*, **629**, L25
- Churchill, C. W., Kacprzak, G. G., Steidel, C. C., et al. 2012, *ApJ*, **760**, 68
- Conroy, C., & Wechsler, R. H. 2009, *ApJ*, **696**, 620
- Cooksey, K. L., Prochaska, J. X., Chen, H.-W., Mulchaey, J. S., & Weiner, B. J. 2008, *ApJ*, **676**, 262
- Cooper, T. J., Simcoe, R. A., Cooksey, K. L., O'Meara, J. M., & Torrey, P. 2015, *ApJ*, **812**, 58
- Crighton, N. H. M., Hennawi, J. F., & Prochaska, J. X. 2013, *ApJL*, **776**, L18
- Danforth, C. W., Keeney, B. A., Tilton, E. M., et al. 2016, *ApJ*, **817**, 111
- Dekker, H., D'Odorico, S., Kaufer, A., Delabre, B., & Kotzlowski, H. 2000, *Proc. SPIE*, **4008**, 534
- Faucher-Giguère, C.-A., Hopkins, P. F., Kereš, D., et al. 2015, *MNRAS*, **449**, 987
- Feigelson, E. D., & Nelson, P. I. 1985, *ApJ*, **293**, 192
- Fitzpatrick, E. L., & Spitzer, L., Jr. 1997, *ApJ*, **475**, 623
- Fox, A. J., Barger, K. A., Wakker, B. P., et al. 2018, *ApJ*, **854**, 142
- Fox, A. J., Lehner, N., Lockman, F. J., et al. 2016, *ApJL*, **816**, L11
- Fox, A. J., Lehner, N., Tumlinson, J., et al. 2013, *ApJ*, **778**, 187
- Fraternali, F., & Binney, J. 2008, *MNRAS*, **386**, 935
- Fukugita, M., Hogan, C. J., & Peebles, P. J. E. 1998, *ApJ*, **503**, 518
- Fumagalli, M., O'Meara, J. M., & Prochaska, J. X. 2011a, *Sci*, **334**, 1245
- Fumagalli, M., O'Meara, J. M., & Prochaska, J. X. 2016, *MNRAS*, **455**, 4100
- Fumagalli, M., Prochaska, J. X., Kasen, D., et al. 2011b, *MNRAS*, **418**, 1796
- Gehrels, N. 1986, *ApJ*, **303**, 336
- Glidden, A., Cooper, T. J., Cooksey, K. L., Simcoe, R. A., & O'Meara, J. M. 2016, *ApJ*, **833**, 270
- Green, J. C., Frøning, C. S., Osterman, S., et al. 2012, *ApJ*, **744**, 60
- Hafen, Z., Faucher-Giguère, C.-A., Anglés-Alcázar, D., et al. 2017, *MNRAS*, **469**, 2292
- Hennawi, J. F., Prochaska, J. X., Burles, S., et al. 2006, *ApJ*, **651**, 61
- Howk, J. C., Ribaldo, J. S., Lehner, N., Prochaska, J. X., & Chen, H.-W. 2009, *MNRAS*, **396**, 1875
- Isobe, T., Feigelson, E. D., & Nelson, P. I. 1986, *ApJ*, **306**, 490
- Jenkins, E. B. 2009, *ApJ*, **700**, 1299
- Jenkins, E. B., & Wallerstein, G. 2017, *ApJ*, **838**, 85
- Kacprzak, G. G., Churchill, C. W., Steidel, C. C., Spitler, L. R., & Holtzman, J. A. 2012, *MNRAS*, **427**, 3029
- Kacprzak, G. G., van de Voort, F., Glazebrook, K., et al. 2016, *ApJL*, **826**, L11
- Kalberla, P. M. W., Burton, W. B., Hartmann, D., et al. 2005, *A&A*, **440**, 775
- Keeney, B. A., Stocke, J. T., Danforth, C. W., et al. 2017, *ApJS*, **230**, 6
- Kereš, D., Katz, N., Fardal, M., Davé, R., & Weinberg, D. H. 2009, *MNRAS*, **395**, 160
- Lanzetta, K. M., Bowen, D. V., Tytler, D., & Webb, J. K. 1995, *ApJ*, **442**, 538
- Lehner, N. 2002, *ApJ*, **578**, 126
- Lehner, N. 2017, *ASSL*, **430**, 117
- Lehner, N., & Howk, J. C. 2011, *Sci*, **334**, 955
- Lehner, N., Howk, J. C., Keenan, F. P., & Smoker, J. V. 2008, *ApJ*, **678**, 219
- Lehner, N., Howk, J. C., Tripp, T. M., et al. 2013, *ApJ*, **770**, 138
- Lehner, N., Howk, J. C., & Wakker, B. P. 2015, *ApJ*, **804**, 79
- Lehner, N., Keenan, F. P., & Sembach, K. R. 2001a, *MNRAS*, **323**, 904
- Lehner, N., O'Meara, J. M., Fox, A. J., et al. 2014, *ApJ*, **788**, 119
- Lehner, N., O'Meara, J. M., Howk, J. C., Prochaska, J. X., & Fumagalli, M. 2016, *ApJ*, **833**, 283
- Lehner, N., Prochaska, J. X., Kobulnicky, H. A., et al. 2009, *ApJ*, **694**, 734
- Lehner, N., Savage, B. D., Richter, P., et al. 2007, *ApJ*, **658**, 680
- Lehner, N., Sembach, K. R., Dufton, P. L., Rolleston, W. R. J., & Keenan, F. P. 2001b, *ApJ*, **551**, 781
- Martin, C. L., Shapley, A. E., Coil, A. L., et al. 2013, *ApJ*, **770**, 41
- Morton, D. C. 2003, *ApJS*, **149**, 205
- Muzahid, S., Kacprzak, G. G., Churchill, C. W., et al. 2015, *ApJ*, **811**, 132
- O'Meara, J. M., Lehner, N., Howk, J. C., et al. 2015, *AJ*, **150**, 111
- O'Meara, J. M., Lehner, N., Howk, J. C., et al. 2017, *AJ*, **154**, 114
- Peebles, M., Tumlinson, J., Fox, A., et al. 2017, The Hubble Spectroscopic Legacy Archive, Instrument Sci. Rep. COS 2017-4 (Baltimore, MD: STScI)
- Penton, S. V., Stocke, J. T., & Shull, J. M. 2002, *ApJ*, **565**, 720
- Prochaska, J. X., Hennawi, J. F., Lee, K.-G., et al. 2013, *ApJ*, **776**, 136
- Prochaska, J. X., Weiner, B., Chen, H.-W., Cooksey, K. L., & Mulchaey, J. S. 2011a, *ApJS*, **193**, 28
- Prochaska, J. X., Weiner, B., Chen, H.-W., Mulchaey, J., & Cooksey, K. 2011b, *ApJ*, **740**, 91
- Prochaska, J. X., & Wolfe, A. M. 1997, *ApJ*, **487**, 73
- Quiret, S., Péroux, C., Zafar, T., et al. 2016, *MNRAS*, **458**, 4074
- Rafelski, M., Wolfe, A. M., Prochaska, J. X., Neeleman, M., & Mendez, A. J. 2012, *ApJ*, **755**, 89
- Ribaldo, J., Lehner, N., Howk, J. C., et al. 2011, *ApJ*, **743**, 207
- Rocha-Pinto, H. J., Scalo, J., Maciel, W. J., & Flynn, C. 2000, *A&A*, **358**, 869
- Rubin, K. H. R., Prochaska, J. X., Koo, D. C., et al. 2014, *ApJ*, **794**, 156
- Savage, B. D., & Sembach, K. R. 1991, *ApJ*, **379**, 245
- Savage, B. D., & Sembach, K. R. 1996, *ARA&A*, **34**, 279
- Sembach, K. R., & Savage, B. D. 1992, *ApJS*, **83**, 147
- Shapley, A. E., Steidel, C. C., Pettini, M., & Adelberger, K. L. 2003, *ApJ*, **588**, 65
- Shull, J. M., Danforth, C. W., Tilton, E. M., Moloney, J., & Stevans, M. L. 2017, *ApJ*, **849**, 106
- Simcoe, R. A., Sargent, W. L. W., & Rauch, M. 2002, *ApJ*, **578**, 737
- Simcoe, R. A., Sargent, W. L. W., & Rauch, M. 2004, *ApJ*, **606**, 92
- Spitzer, L. 1978, *Physical Processes in the Interstellar Medium* (New York: Wiley)
- Steidel, C. C., Erb, D. K., Shapley, A. E., et al. 2010, *ApJ*, **717**, 289
- Stevans, M. L., Shull, J. M., Danforth, C. W., & Tilton, E. M. 2014, *ApJ*, **794**, 75
- Tejos, N., Morris, S. L., Finn, C. W., et al. 2014, *MNRAS*, **437**, 2017
- Telfer, R. C., Zheng, W., Kriss, G. A., & Davidsen, A. F. 2002, *ApJ*, **565**, 773
- Tripp, T. M., Meiring, J. D., Prochaska, J. X., et al. 2011, *Sci*, **334**, 952
- Tumlinson, J., Peebles, M. S., & Werk, J. K. 2017, *ARA&A*, **55**, 389
- Tumlinson, J., Thom, C., Werk, J. K., et al. 2011, *Sci*, **334**, 948
- Tumlinson, J., Thom, C., Werk, J. K., et al. 2013, *ApJ*, **777**, 59
- Turner, M. L., Schaye, J., Crain, R. A., et al. 2017, *MNRAS*, **471**, 690
- van de Voort, F., & Schaye, J. 2012, *MNRAS*, **423**, 2991
- van de Voort, F., Schaye, J., Altay, G., & Theuns, T. 2012, *MNRAS*, **421**, 2809
- Verner, D. A., Barthel, P. D., & Tytler, D. 1994, *A&AS*, **108**, 287
- Vogt, S. S., Allen, S. L., Bigelow, B. C., et al. 1994, *Proc. SPIE*, **2198**, 362
- Wakker, B. P. 2001, *ApJS*, **136**, 463
- Wakker, B. P., Hernandez, A. K., French, D. M., et al. 2015, *ApJ*, **814**, 40
- Weiner, B. J., Coil, A. L., Prochaska, J. X., et al. 2009, *ApJ*, **692**, 187
- Welty, D. E., Frisch, P. C., Sonneborn, G., & York, D. G. 1999a, *ApJ*, **512**, 636
- Welty, D. E., Hobbs, L. M., Lauroesch, J. T., et al. 1999b, *ApJS*, **124**, 465
- Welty, D. E., Lauroesch, J. T., Blades, J. C., Hobbs, L. M., & York, D. G. 1997, *ApJ*, **489**, 672
- Werk, J. K., Prochaska, J. X., Thom, C., et al. 2013, *ApJS*, **204**, 17
- Werk, J. K., Prochaska, J. X., Tumlinson, J., et al. 2014, *ApJ*, **792**, 8
- White, S. D. M., & Rees, M. J. 1978, *MNRAS*, **183**, 341
- Wotta, C. B., Lehner, N., Howk, J. C., et al. 2018, *ApJ*, submitted
- Wotta, C. B., Lehner, N., Howk, J. C., O'Meara, J. M., & Prochaska, J. X. 2016, *ApJ*, **831**, 95